Rapid metabolic regulation of a novel arginine methylation of KCa3.1 attenuates T cell exhaustion.

Authors:

Piyush Sharma[1*], Ao Guo[1#], Suresh Poudel[1], Emilio Boada-Romero[1], Katherine C. Verbist[1], Gustavo Palacios[1], Kalyan Immadisetty[2], Mark J. Chen[1,3], Dalia Haydar[4], Ashutosh Mishra[5], Junmin Peng[5,6], M. Madan Babu[2], Giedre Krenciute[4], Evan S. Glazer[7], Douglas R. Green[1*].

[1]Department of Immunology, St. Jude Children's Research Hospital, Memphis, TN 38105, USA

[2]Center of Excellence in Data Driven Discovery, Department of Structural Biology, St. Jude Children's Research Hospital, Memphis, TN 38105, USA

[3]Department of Laboratory Medicine, Cleveland Clinic, Cleveland, OH 44106, USA

[4]Department of Bone Marrow Transplantation and Cellular Therapy, St. Jude Children's Research Hospital, Memphis, TN 38105, USA

[5]Center for Proteomics and Metabolomics, St. Jude Children's Research Hospital, Memphis, TN 38105, USA

[6]Department of Structural Biology, Department of Developmental Neurobiology, St. Jude Children's Research Hospital, Memphis, TN 38105, USA

[7]Department of Surgery, University of Tennessee Health Science Center, 910 Madison Ave., Suite 300, Memphis, TN 38163, USA

[#]Current address: Key Laboratory of Immune Response and Immunotherapy, School of Basic Medical Sciences, Division of Life Sciences and Medicine, University of Science and Technology of China, Hefei 230027, Anhui, China

*Corresponding author: piyush.sharma@stjude.org, douglas.green@stjude.org

ABSTRACT

T cell exhaustion is linked to persistent antigen exposure and perturbed activation events, correlating with poor disease prognosis. Tumor-mediated T cell exhaustion is well documented; however, how the nutrient-deprived tumor niche affects T cell receptor (TCR) activation is largely unclear. We show that methionine metabolism licenses optimal TCR signaling by regulating the protein arginine methylome, and limiting methionine availability during early TCR signaling

promotes subsequent T cell exhaustion. We discovered a novel arginine methylation of a Ca^{2+}-activated potassium transporter, KCa3.1, prevention of which results in increased Ca^{2+}-mediated NFAT1 activation, NFAT1 promoter occupancy, and T cell exhaustion. Furthermore, methionine supplementation reduces nuclear NFAT1 in tumor-infiltrating T cells and augments their anti-tumor activity. These findings demonstrate metabolic regulation of T cell exhaustion determined during TCR engagement.

Main Text

To provide an effective anti-tumor response, $CD8^+$ T cells are activated in draining lymph nodes (dLN) and within the nutrient-deprived tumor microenvironment (TME) (*1, 2*). The TME is a constraining niche that leads to defective cytotoxic function of $CD8^+$ T cells and tumor evasion, at least in part by promoting T cell exhaustion (*3, 4*). T cell exhaustion is a differentiation state characterized by a loss of proliferative capacity and a reduction in effector molecules(*5*). To date, T cell exhaustion has been described as being the result of chronic antigen exposure and associated changes in specific epigenetic signatures (*6*). Recent studies, however, have shown that T cells can acquire an exhaustion signature early after activation (*7*), which raises the possibility that the exhaustion program is driven by factors that occur early after activation in addition to chronic antigen exposure.

T cell receptor (TCR) engagement is stringently regulated to ensure optimal activation. TCR activation leads to a rapid increase in metabolic and proliferative capacities that are necessary for T cell function and expansion. Metabolic flux during TCR engagement is crucial, and changes in extracellular nutrient availability have been shown to modulate T cell activation (*8*). Activation of T cells within the TME is vital for an effective anti-tumor response (*2*), an environment known for its paucity of nutrients. It is therefore likely that nutrient metabolites play a role in optimal TCR activation. One such metabolite, Methionine (Met), is known to be crucial for epigenetic and proteomic maintenance and is among the amino acids depleted in the TME. Tumor cells act as a Met sink, depriving T cells, and supplementation of Met enhances anti-tumor immunity (*9*). It is unclear, however, how reduced levels of extracellular Met affect TCR-mediated T cell activation and eventual fate.

63 **Results**

64 **Early methionine limitation promotes T cell exhaustion.**

65 To determine which amino acids were rapidly consumed upon T cell activation and whether Met
66 was among them, we activated OT-I transgenic $CD8^+$ T cells in complete medium and performed
67 targeted mass spectrometry. We observed a significant decrease in intracellular Met and other
68 amino acids in only 10 min (Fig. 1A). Among the amino acids important for T cells, Met is the
69 sole amino acid responsible for cellular methylome maintenance via the S-adenosyl Met (SAM)
70 pathway, and alterations in the SAM pathway adversely affect T cell function (*10, 11*). In complete
71 media, no significant changes were observed in SAM or S-adenosyl homocysteine (SAH) (Fig.
72 1B, upper panel). Instead, T cells consumed the intracellular Met pool only in Met-deprived
73 medium, correlating with decreases in SAM concentrations and corresponding increases in SAH
74 (Fig.1B, bottom panel). These observations indicate that extracellular Met is required to maintain
75 the SAM cycle during T cell activation. By fueling their own rapid proliferation (*12*), tumor cells
76 act as nutrient sinks, creating a nutrient-deprived niche for T cells. To determine whether tumor
77 cells deplete Met in this T cell niche, we cultured $CD8^+$ T cells along with B16f10 (B16) melanoma
78 cells in a trans-well system and analyzed the amino acid profile in a time-dependent fashion. We
79 observed that tumor cells consume Met (and other amino acids), reducing availability for T cells
80 and diminishing the intracellular pool (Fig. S1A, Table. 1). Furthermore, mass spectrometric
81 analysis of tumor-infiltrating $CD8^+$ lymphocytes ($CD8^+$ TIL) and draining lymph node (dLN)
82 $CD8^+$ T cells from B16 subcutaneous tumor-bearing mice at day 9 revealed a ~50% reduction in
83 intracellular Met in $CD8^+$ TIL compared to that in dLN $CD8^+$ T cells (Fig. 1C and Fig. S1B). We
84 also observed a similar decrease in intracellular Met in $CD8^+$ TIL isolated from primary human
85 colorectal carcinomas compared with corresponding $CD8^+$ T cells from PBMC (Fig. 1D) and
86 compared with that of the tumor cells themselves (Fig. S1C).

87

88 $CD8^+$ T cells are activated in both secondary lymphoid tissues and within tumors(*1, 13*). Thus,
89 upon tumor infiltration, $CD8^+$ T cells will experience antigen presentation in a nutrient-deficient
90 microenvironment. To determine whether Met limitation during early TCR engagement affects T
91 cell proliferation, we lowered the available amount of Met to 0.03 mM in the culture medium,
92 approximately half that of murine serum (~0.061mM). Cell-trace violet (CTV) labelled OT-I $CD8^+$
93 T cells were activated in media with control (0.1 mM) or 0.03 mM Met for 30 min to 6 hr, after

94 which Met was restored to 0.1 mM, and we observed no difference in the proliferation of T cells
95 activated in reduced Met for different times (Fig. S1D). Upon transferring these activated T cells
96 into *Rag1*$^{-/-}$ mice bearing B16 tumors expressing ovalbumin (B16-OVA) 24 h after activation (Fig.
97 S1E), we observed defective tumor control in T cells activated in 0.03mM Met compared to 0.1
98 mM Met, across all time points, with the earliest being 30 min (Fig. S1F). Next, we generated
99 LCMV-GP33 specific memory T cells (Fig. S1G) and activated them for 24 hrs with GP33 peptide
100 in either 0.1 mM Met or 0.03 mM Met for 30 min, after which Met was restored to 0.1 mM and
101 then transferred them into B16-GP33 (B16 expressing GP33 peptide) tumor-bearing *Rag1*$^{-/-}$ mice.
102 We observed defective tumor control leading to poor survival in mice receiving T cells activated
103 in 0.03 mM Met compared to 0.1 mM Met (Fig. S1H and I). We then activated OT-I CD8^{+} T cells
104 in either 0.1 mM or 0.03 mM Met for 30 min as previously and transferred into B16-OVA tumor-
105 bearing *Rag1*$^{-/-}$ or C57BL6/J (WT) mice. We again observed that T cells activated in 0.03 mM Met
106 for the initial 30 min presented with defective tumor control and resultant poor survival of the
107 recipient animals (Fig. 1E and Fig. S1J). Further analysis of these same animals revealed increased
108 tumor burden at day 9, a reduction in CD62L^{+}, CD62L^{hi}CD44^{hi} central memory cells (Tcm),
109 increased TOX expression in T cells, and reduced IFNγ production (Fig. S1K, L and M).
110
111 T cell exhaustion is known to contribute to poor prognoses in cancer patients(*14*). This
112 dysfunctional state is at least in part driven by the transcription factor TOX and is accompanied by
113 markers such as increased surface expression of PD1 and Tim-3 and reduced effector cytokine
114 production(*5, 15*). To examine exhaustion here we activated CD45.1^{+} or CD45.2^{+} OT-I CD8^{+} T
115 cells in 0.1 (control) or 0.03 mM Met for 30 min, restored Met to 0.1 mM for 24 hrs, and mixed
116 them at a ratio of 1:1 before transferring them into B16-OVA tumor-bearing *Rag1*$^{-/-}$ mice (Fig.
117 1F). Even though CD8^{+} TIL initially activated in 0.03mM outnumbered the 0.1 mM-activated
118 CD8^{+} TIL at day 12 (Fig. S2A), these cells exhibited significant increases in exhaustion-associated
119 expression of PD1 and Tim-3 (Fig. 1G) and TOX (Fig. 1H), reduced TCF-1 expression (Fig. S2B),
120 and reduced effector cytokines (Fig. 1I).
121
122 Exhausted T cells have been further defined as precursors of exhaustion (TEXprog) and
123 TEXprogenitor-like cells, which both produce a replicative burst and effector function upon
124 checkpoint blockade (*16*), and terminally exhausted cells (TEXterm), which fail to mount an

125 effective effector response (*17, 18*). Although TOX is associated with maintenance of exhausted
126 T cells, it is also expressed in TEXprog (*19*). We therefore further dissected the TOX$^+$ CD8$^+$ T
127 cells from Fig. 1H and found decreased TEXprog (TCF1$^+$Tim-3$^-$) and increased TEXterm (TCF1$^-$
128 Tim-3$^+$) among T cells initially activated in 0.03 mM Met, suggesting a decreased pool of stem-
129 like TEXprog cells (Fig. S2C and D). Furthermore, evaluation of total CD8$^+$ TILs from mice
130 receiving T cells activated in 0.03 mM Met revealed a lower frequency of TEXprog cells as
131 TCF1$^+$Tim-3$^-$ (Fig. 1J), Tim-3$^-$Ly108$^+$ (Fig. S1E), CX3CR1$^+$Ly108$^+$ TEXprogenitor-like cells
132 (Fig. 1K) and a corresponding increase in frequency of TEXterm cells defined by TCF1$^-$Tim-3$^-$
133 (Fig. 1L), Tim-3$^+$Ly108$^-$ and CXCR3$^-$Tim-3$^+$ (Fig. S2F). We also observed a decrease in memory-
134 associated markers such as CD62L$^+$, CD62L$^+$CD44$^+$ (Fig. S2G) and CD127$^+$CD27$^+$ (Fig. S1H and
135 I) and an increase in KLRG1$^+$CD127$^-$ terminal effector-like T cells when initially activated in 0.03
136 mM Met (Fig. S1J and K).
137
138 To examine the transcriptomic state, we performed global RNA-seq of day 9 TIL from T cells
139 originally activated for 30 min in 0.1 mM or 0.03 mM Met and then cultured in 0.1 mM Met for
140 24hrs prior to transfer into B16-OVA tumor-bearing mice. We found several transcriptomic
141 changes, the majority of which being increased expression of differentially enriched (DE) genes
142 in T cells initially activated in 0.03 mM Met (Fig. S3A and B). Over-representation analysis of the
143 DE genes in T cells activated in 0.1 mM Met revealed enrichment of GOBP pathways which are
144 associated with T cell effector functions along with increases in transcription factors associated
145 with a stem-like T cell state and memory generation(*20-23*) (Fig. S3C). Similar analysis of cells
146 initially activated in 0.03 mM Met showed enrichment of genes which are associated with terminal
147 differentiation or dysfunction of T cells and transcription factors associated with hyperactivation
148 and development and maintenance of T cell exhaustion(*24-27*) (Fig. S3D). GSEA analysis also
149 showed an enriched exhaustion-associated gene set (*28, 29*) in CD8$^+$ TIL initially activated in 0.03
150 mM Met (Fig. 1M) and enrichment of hallmark gene sets associated with T cell effector function
151 in control T cells (Fig. S3E). These results suggest that Met availability during initial TCR
152 engagement influences T cell differentiation, with initial, reduced Met availability promoting
153 hyperactivation and driving T cells towards exhaustion.
154
155 **Methionine regulated Ca^{2+} flux induces NFAT1.**

156 Among the earliest events in T cell activation is the influx of Ca^{2+} (*30*). This is accompanied by
157 the activation of calcineurin, which dephosphorylates nuclear factor of activated T cells 1
158 (NFAT1), resulting in its nuclear translocation and activation (*31*). Because low Met levels for
159 only the first 30 min of activation influenced the T cell phenotype, we investigated changes in Ca^{2+}
160 flux using Fluo-8. We observed increased Ca^{2+} influx upon stimulation of T cells with anti-
161 CD3/CD28 antibody in 0.03 mM compared to 0.1 mM Met (Fig. 2A). NFAT1 cooperates with the
162 AP1 complex to ensure optimal T cell activation and differentiation, but high levels of NFAT1
163 activity have been associated with T cell dysfunction and exhaustion (*31, 32*). Confocal imaging
164 revealed an increase in activated NFAT1(nuclear localization of NFAT1) in T cells 30 min
165 activated with anti-CD3/28 in 0.03 mM Met compared to 0.1 mM Met (Fig. 2B, Fig. S4A),
166 quantified as either a ratio of nuclear NFAT1 to whole cell NFAT (Fig. 2C and S4C(0.0 mM Met))
167 or as nuclear NFAT1 fluorescence intensity (Fig. S4B), which were abolished upon treatment with
168 either the calcineurin inhibitor Cyclosporin A (CsA) (Fig. 2B and C) or the CRAC channel
169 inhibitor YM-58483 (Fig. S4D and E). We then activated $CD8^+$ T cells in complete medium for
170 24hrs and rested them for 48hrs before secondary activation in 0.03 mM or 0.1 mM Met and
171 observed increased nuclear NFAT1 levels in 0.03 mM Met 30 min after activation (Fig. S4F),
172 suggesting that the effect of limiting Met on NFAT1 activation is independent of previous
173 activation events. We also examined NFAT2 at 30 min post activation and found no difference in
174 its activation in T cells activated in either 0.1 mM or 0.03 mM Met (Fig. S4G).
175
176 NFAT1 is known to regulate several exhaustion associated genes such as *Lag3, Pdcd1, Havcr2,*
177 *Ctla4, Tnfrsf9 (32)*. We performed NFAT1 CUT&RUN on T cells activated in 0.1 mM or 0.03
178 mM Met for 30 min, followed by 0.1 mM Met for 24hrs and observed more reads in the low Met
179 group (Fig. 2D). Met limitation for the initial 30 min resulted in increased binding of NFAT1 to
180 *Lag3, Pdcd1, Havcr2, Ctla4, Tnfrsf9, and Tox* gene loci (Fig. 2E and S4H), which also correlated
181 with increased transcription of these genes (Fig. S4I). Altogether, our results suggest that reduced
182 Met availability during the initial stages of TCR activation directs the trajectory of T cells towards
183 hyperactivation and eventually exhaustion, and the maintenance of extracellular Met levels in the
184 face of rapid Met consumption upon TCR engagement regulates Ca^{2+}-mediated NFAT1 activity
185 and T cell fate.
186

187 **KCa3.1 methylation regulates NFAT1.**

188 Methionine metabolism is the sole pathway for epigenetic and proteomic methylome maintenance,
189 which is known to affect T cell function(*9*). When converted to SAH, SAM acts as the methyl
190 donor; thus, the ratio of SAM to SAH is known as the cellular methylation potential (*33*), an index
191 of a cell's capacity to maintain its methylome. We calculated the SAM/SAH ratio over time after
192 TCR engagement in the absence of extracellular Met and found this ratio to be significantly
193 reduced as early as 10 min post-activation (Fig. S5A), suggesting alterations in the methylome.
194 Met metabolism is essential for DNA methylation (*34*); however, we found no significant
195 differences in global 5-methylcytosine levels at either 30 min or 24 hrs in T cells activated as above
196 (Fig. S5B). We similarly assessed H3me3K27 and H3me2K4 by CUT&RUN at 24 hrs post
197 activation, but again, no global changes were observed (Fig. S5C and D). Thus, Met restriction for
198 only the first 30 min of T cell activation does not appear to directly affect global DNA or histone
199 methylation.

200

201 Therefore, we postulated that Met restriction influences early methylation events independently of
202 DNA and histone methylation. Post-translational protein arginine methylation mediated by protein
203 arginine methyltransferases regulates protein function(*35, 36*). We found that arginine methylation
204 in T cells activated in 0.0 mM or 0.03 mM Met was significantly reduced 30 min post-activation
205 when compared to T cells activated in 0.1 mM Met (Fig. S5E and Fig. 3A). To identify specific
206 proteins differentially methylated upon TCR engagement in limited Met, $CD8^+$ T cells activated
207 for 30 min were processed for methyl-arginine immunoprecipitation and quantification using
208 multiplexed tandem mass tag-mass spectrometry (TMT-MS). We identified common proteins
209 which were differentially methylated in 0.0 mM and 0.03 mM Met activation conditions compared
210 to 0.1 mM Met (Fig. S5F) and found the top candidate, KCa3.1, to be less methylated at Arginine-
211 350 (R350) (Fig. S5G). Furthermore, protein-BLAST analysis showed that KCa3.1 R350 is
212 conserved across species, including humans, which suggested that R350 may be important for
213 KCa3.1 regulation (Fig. S5H).

214

215 KCa3.1 is a calcium-activated potassium transporter encoded by *Kcnn4* and is activated by
216 calmodulin binding upon TCR-mediated Ca^{2+} flux (*37*) (Fig. S5I). During T cell activation, the
217 plasma membrane is hyperpolarized to ensure sufficient Ca^{2+} flux for optimal signaling (*38*), and

218 this is maintained by K^+ efflux through potassium transporters such as KCa3.1 (*39, 40*). Based on
219 our earlier observation of increased Ca^{2+} signaling, we hypothesized that R350 methylation of
220 KCa3.1 limits its activity, and loss of this methyl group may result in hyperactivation, leading to
221 increased Ca^{2+} influx and NFAT1 activation. To test this, we used the chemical inhibitor TRAM-
222 34 to reduce KCa3.1 activity (*41, 42*) during T cell activation and observed reduced Ca^{2+} flux upon
223 TRAM-34 treatment only in 0.03 mM Met and not in 0.1 mM Met (Fig. 3B) at the concentration
224 of TRAM-34 we employed. Measurement of nuclear NFAT1 levels showed that the treatment
225 normalized nuclear NFAT1 levels in T cells activated in 0.03 mM Met in a dose-dependent manner
226 and had no effect on T cells activated in 0.1 mM Met (Fig. S6A and B). We then activated OT-I T
227 cells in 0.1 mM or 0.03 mM Met with either DMSO or TRAM-34 for 30 min and then cultured
228 the cells for an additional 24 hrs in 0.1 mM Met before transferring into B16-OVA tumor-bearing
229 $Rag1^{-/-}$ mice. Chemical inhibition of KCa3.1 for 30 min significantly improved anti-tumor activity
230 in T cells activated for 30 min in 0.03 mM Met (Fig. 3C), suggesting that KCa3.1 activity
231 influences T cell function.
232
233 **Methylation-deficient KCa3.1 increases NFAT1 activation.**
234 To specifically interrogate the role of R350 methylation of KCa3.1 in T cell activation, we cloned
235 KCa3.1 ($Kca3.1^{WT}$) and a mutant with an alanine substitution ($KCa.3.1^{R350A}$) into retroviral vectors
236 and expressed them in primary murine $CD8^+$ T cells in which endogenous KCa3.1 was deleted
237 using CRISPR/Cas9 (Fig. S6C, D and E), and expression of the two was similar (Fig. S6F). Ca^{2+}
238 flux analysis using ICR-1 AM showed increased flux upon activation in $KCa3.1^{R350A}$ T cells (Fig.
239 3D) with concordant increases in nuclear NFAT1 30 min post activation (Fig. 3E, F and Fig. S6G).
240 This heightened nuclear NFAT1 in cells expressing $KCa3.1^{R350A}$ was visible under basal
241 conditions increased upon activation in a time-dependent manner (Fig. S6H).
242
243 To better understand how arginine methylation mechanistically modulates KCa3.1 activity, we
244 performed MD simulations with the solved crystal structure of human KCa3.1(hKCa3.1) bound to
245 calmodulin (CaM) at R352, corresponding to R350 in murine KCa3.1 (Fig. S7A). The calmodulin
246 binding pocket encompasses D78-T79-D80-S81-E82-E83-E84, which is predominantly
247 negatively charged/polar, where E84 forms a salt bridge with R352 of hKCa3.1. Our results
248 showed that both symmetrical di-methylation (SDMA) and asymmetrical di-methylation (ADMA)

249 of R352 introduced a hydrophobic methyl group into this negatively charged/polar CaM binding
250 pocket, thereby weakening the hKCa3.1 and CaM interaction (Fig. S7B). Furthermore, MD
251 simulations showed that the salt bridge interaction of R352 with E84 of the CaM binding pocket
252 diminished over time, especially in the case of SDMA where both guanidino nitrogens are
253 methylated, compared to ADMA in which only one nitrogen is methylated (Fig. S7C), suggesting
254 that disruption of arginine methylation promoted stabilization of calmodulin binding, leading to
255 increased activation of the channel and Ca^{2+} flux, consistent with our experimental observations.
256
257 To investigate whether the genomic state of T cells activated in reduced Met is similar to those
258 with mutant KCa3.1, we analyzed global chromatin accessibility via ATAC-Seq after 24 hrs of *in-*
259 *vitro* activation of T cells initially activated in 0.1 mM or 0.03 mM Met and T cells expressing WT
260 or mutant KCa3.1. This analysis showed a separation of groups in principle component analysis
261 (PCA), suggesting distinct phenotypes (Fig. S8A and B) with significantly more accessible regions
262 in T cells initially activated in 0.03 mM Met, similar to KCa3.1^{R350A} T cells (Fig. S8C). Upon
263 comparing the ATAC-Seq results, we found several common differentially accessible regions
264 (DAR) (Fig. S8D) with enrichment of gene sets associated with T cell exhaustion (Fig. S8E).
265 HOMER motif analysis was similarly enriched in exhaustion-associated motifs (*24*) in both
266 ATAC-Seq and the common DAR (Fig. S8F). Furthermore, GSEA of ATAC-Seq of WT or mutant
267 KCa3.1-expressing T cells revealed enrichment of GOBP terms associated with negative
268 regulators of T cell-mediated immunity and gene sets associated with T cell exhaustion (*28, 29*) in
269 T cells expressing mutant KCa3.1^{R350A} (Fig. S8G and H), suggesting that ablation of R350
270 methylation drives T cells towards exhaustion early after activation. Despite these results,
271 KCa.3.1^{R350A} did not fully phenocopy the chromatin effects of activation in 0.03 mM Met,
272 suggesting that differentially methylated proteins in addition to KCa.3.1 may also impact
273 chromatin accessibility following activation in the latter condition.
274
275 **Ablation of KCa3.1 methylation promotes T cell exhaustion.**
276 To examine the consequences of ablation of R350 methylation *in vivo*, we transferred T cells
277 expressing KCa.3.1^{WT} or KCa.3.1^{R350A} into B16-OVA tumor-bearing Rag1$^{-/-}$ mice. We found that
278 T cells expressing KCa.3.1^{R350A} displayed impaired tumor control with less survival of recipient
279 animals (Fig. 3G and H). Tumors were isolated at day 12 post-T cell injection, and consistently,

280 much larger tumors were extracted from animals treated with T cells expressing KCa.3.1^{R350A} (Fig.
281 3I and Fig. S9A). KCa.3.1^{R350A}-expressing TIL showed high surface expression of the exhaustion
282 markers PD1, Lag3 and Tim-3 (Fig. S9B) that correlated with increased TOX expression (Fig.
283 S9C). Among these cells we also found fewer TEXprog (CD69^{lo}Ly108^{hi})(*43*) and IFNγ- and
284 TNFα-producing T cells (Fig. S9D and E). Next, we performed a similar experiment in a
285 competitive setting, wherein CD45.1^{+} KCa.3.1^{WT} and CD45.1^{+}CD45.2^{+} Kca.3.1^{R350A}-expressing
286 OT-I CD8^{+} T cells were mixed at a 1:1 ratio and transferred into B16-OVA tumor-bearing *Rag1*$^{-/-}$
287 mice (Fig. 3J). TIL analysis at D12 showed increased PD1^{+}Tim-3^{+}, Eomes^{+}PD1^{+} and TOX
288 expression in Kca.3.1^{R350A} T cells, which correlated with reduced expression of the effector
289 cytokines IFNγ and TNFα (Fig. 3K, L and Fig. S9F). Further analysis revealed a decreased
290 frequency of TCF1^{+}Tim3^{-} TEXprog and increased TCF1^{-}Tim-3^{+} TEXterm populations (Fig. 3M
291 and Fig. S9G). We also observed a decrease in CD62L^{+} and CD127^{+}CD27^{+} memory T cells (Fig.
292 S9H) with an increase in the KLRG1^{+}CD127^{-} terminal effector-like phenotype in KCa.3.1^{R350A}-
293 expressing T cells (Fig. S9I).
294
295 In addition to tumors, T cell exhaustion is also a prominent feature of chronic viral infection (*44*).
296 We utilized the Lymphocytic-Choriomeningitis Virus (LCMV) infection system and infected WT
297 mice containing CD45.1^{+}CD45.2^{+} KCa.3.1^{WT} and CD45.2^{+} KCa.3.1^{R350A}-expressing Thy1.1^{+} P14^{+}
298 T cells at a 1:1 ratio into mice, which were infected with either an acute Armstrong or a chronic
299 Clone-13 strain, and their spleens were analyzed on day 9 post-infection (Fig. 3N). The
300 KCa.3.1^{R350A} population frequency was significantly reduced in Clone-13 infection, but no
301 significant change was observed in acute infection (Fig. S9J). In both acute and chronic infections,
302 KCa.3.1^{R350A}-expressing P14^{+} T cells displayed increased KLRG1^{+}CD127^{-} terminal effector-like
303 cells and a concurrent decrease in KLRG1^{-}CD127^{+} memory precursor cells (Fig. S9K, L and M).
304 KCa.3.1^{R350A}-expressing T cells also presented with increased TOX, PD1 and Tim3 expression
305 (Fig. 3O and P). Furthermore, we found that KCa.3.1^{R350A}-expressing T cells harbored reduced
306 frequencies of CX3CR1^{+}PD1^{+} TEXprog cells and increased Tim-3^{+}Cx3CR1^{+}PD1^{+} TEXeff and
307 TCF1^{-}Tim3^{+} TEXterm cells, especially in the setting of chronic infection (Fig. 3Q, R and S). Thus,
308 ablation of R350 methylation drives T cells towards exhaustion trajectory even at the early stages
309 of infection. Together, these experiments show that R350 methylation maintains optimal KCa3.1

310 function, ensuring optimal T cell activation and effector function in both tumors and viral
311 infections.
312
313 **Acute Met supplementation promotes anti-tumor T cell function.**
314 To determine whether $CD8^+$ TIL in the TME (where Met is limited) also showed increased nuclear
315 NFAT1, we sorted activated $CD44^+$ $CD8^+$ T cells from B16 tumors and respective dLN at day 9
316 post implantation and imaged for NFAT1. We observed increased levels of nuclear NFAT1 in
317 $CD44^+CD8^+$ TIL compared to counterparts from dLN (Fig. 4A), suggesting that reduced Met
318 availability in the TME may have led to increased NFAT1 activation in those T cells. Continuous
319 Met supplementation in tumors has been shown to promote anti-tumor T cell activity by promoting
320 global epigenetic maintenance (*9*). Our findings, however, highlight an early role for Met in T cell
321 fate, and we hypothesized that Met supplementation up to that of serum levels would increase T
322 cell anti-tumor activity at the early stages of tumor development. We therefore injected 50 µl of
323 61µM Met peri-tumorally once per day for 5 days when tumor volumes were 70-100 mm^3 (Fig.
324 S10A) and found that treatment decreased nuclear NFAT1 levels in $CD44^+$ $CD8^+$ TIL as compared
325 to TIL from HBSS-injected tumors (Fig. 4B). Indeed, nuclear NFAT1 in TIL was similar to or
326 lower than that in $CD8^+$ T cells from dLN (Fig. S10B). Furthermore, acute Met supplementation
327 delayed tumor growth in multiple murine tumor models, thereby improving overall survival (Fig.
328 3C, D; Fig. S10C, D and E). Met supplementation resulted in decreased PD1, Tim3, and CD69
329 surface expression (Fig. S10F) along with increased $CD62L^{hi}CD44^{hi}$ Tcm and reduced
330 $CD62L^{lo}CD44^{hi}$ Tem (Fig. S10G) compared to TIL in HBSS-treated tumors. In contrast to
331 immunocompetent WT mice, Met injected peri-tumorally in tumor-bearing NSG mice resulted in
332 no difference in tumor growth (Fig. S10H), implying a lymphocyte-mediated effect. Depletion
333 with an anti-CD8 antibody (Fig. S10I) in B16-OVA tumor-bearing mice abrogated the effect of
334 Met supplementation on tumor control (Fig. 3E). We then employed a contralateral tumor model
335 with B16-OVA implanted in one shoulder and in the opposite abdominal flank and injected Met
336 peri-tumorally to the latter tumor and Met supplementation of the abdominal tumors impeded
337 contralateral tumor growth (Fig. S10J and K), further indicating a specific T cell response. We
338 also found that dietary Met supplementation in B16 tumor-bearing mice showed better tumor
339 growth control (Fig. S10L), which is concordant with a recent study showing that Met

340 supplementation in humans increased the effector function of $CD8^+$ T cells(*9*). Met
341 supplementation, therefore, enhances the anti-tumor function of $CD8^+$ T cells.
342
343 **Acute Met supplementation enhances ICB and CAR treatment.**
344 Immune checkpoint blockade (ICB) has been widely used either alone or in combination with
345 cancer treatments (*45*). To query whether Met supplementation might cooperate with ICB, we
346 administered either IgG isotype or anti-PD1 antibody along with HBSS or Met supplementation
347 in subcutaneous MC38 tumor-bearing mice (Fig. 4F) and found that Met plus anti-PD1 treatment
348 resulted in significantly reduced tumor growth and increased survival of these animals compared
349 to controls (Fig. 3G and H). CAR-T cell treatment has been clinically successful in the treatment
350 of hematological malignincies, but less so in solid tumors (*46, 47*). In a solid tumor model (*48*) in
351 $RAG1^{-/-}$ mice, we supplemented Met in the presence of transferred murine B7-H3 CAR-T cells in
352 a $B7\text{-}H3^+$ F420 (Fig. 4I), and this too improved tumor control and animal survival (Fig. 4J and K).
353
354 **Discussion**
355 T cell exhaustion is generally understood to be a consequence of persistent antigen stimulation (*5,*
356 *44*); however, situations exist in which antigen persistence does not result in exhaustion, such as
357 in autoimmune T cells in Type I diabetes (*23*). It is therefore possible that in addition to chronic
358 antigen exposure, nutrient limitation drives exhaustion (*49, 50*). A recent study suggested that T
359 cells can follow an exhaustion trajectory within hours of antigen recognition (*7*). Here, we propose
360 that the state of T cell exhaustion is the result of a multifactorial pathway that involves the
361 assimilation of different input signals and is engaged as early as the initial cognate antigen
362 recognition.
363
364 Studies have shown that strong TCR signals result in hyperactivation and activation-induced cell
365 death, whereas weak TCR signals result in dampened responses (*51*). NFAT family members are
366 key regulators of T cell activation and interact with key partners to induce activation-associated
367 genes including effector- and exhaustion-associated genes (*52*). Continuous or partner-less NFAT
368 activation is associated with hyperactivation, anergy and exhaustion (*31, 32, 53*); therefore, NFAT
369 activation must be tightly controlled for optimal T cell function, but little is known about how
370 niche-specific nutrients regulate NFAT. We show that during rapid tumor proliferation in the early

growth phase, $CD8^+$ TIL display increased NFAT1 activation, which is regulated metabolically. Our data provide a novel mechanism of Met metabolism in the regulation of NFAT1 activation via post-translational modification of KCa3.1, without which $CD8^+$ T cells progresses towards exhaustion. We found that arginine methylation in KCa3.1 limits Ca^{2+}-dependent NFAT1 signaling, ensuring optimal activation in tumors and infections. Met supplementation to the TME preserves anti-tumor immunity (*9*) and limits exhaustion (this study), a treatment that can be harnessed to improve patient prognosis in combination with ICB therapies. Our results emphasize the importance of non-histone protein methylation in the functional maintenance of T cells in diseases and describe a link between TCR signaling, metabolic regulation, and transcription factor activation. These results suggest a change in the current dogma of T cell exhaustion from a state driven by persistent antigen exposure—acquired over a long period of time—to a dynamic state controlled by multiple pathways over the course of T cell activation and differentiation. Our study demonstrates that metabolism-dependent, rapid proteomic modifications that occur upon TCR engagement influence subsequent T cell fate and provides mechanistic insight into how niche-specific nutrient deprivation renders T cells dysfunctional.

Acknowledgements: We thank P. Fitzgerald, S. Sirasanagandla, M. Yang and L. Harris, for technical and administrative assistance; L. Long and H. Chi for providing retroviral vectors and Cas9-OTI mice; C. Guy for microscope imaging assistance; M. Morrison for organizing patient samples; the staff at the St. Jude Immunology Flow Cytometry Core Facility for cell sorting. We thank Dr. S. Pounds for additional assistance with the statistical analysis of the data in Fig. 4B. Statistical calculations were performed using GraphPad Prism. Illustrations were created using BioRender software.

Funding: This worked in supported by National Institutes of Health grants AI123322 and CA231620 (D.R.G.), American Lebanese Syrian Associated Charities (ALSAC) (G.K.) and National Cancer Institute grant K99CA256262 (D.H.)

Author Contributions

Conceptualization: PS

Methodology: PS, AG, GP, AM, JP, MMB, GK, ESG, DRG

402 Investigation: PS, AG, EBR, GP, KCV, KI, AM, DH

403 Visualization: PS, SP, MJC

404 Software: SP, MJC

405 Supervision: DRG

406 Funding acquisition: DRG, DH, GK

407 Writing – original draft: PS, DRG

408 Writing – review & editing: PS, KCV, DRG

409 **Competing Interests:** D.R.G. consulted for Venus Therapeutics, Boehringer-Ingelheim and
410 Asha Pharmaceuticals. E.S.G consulted for Anviron. G.K. has patent applications in field of cell
411 or gene therapy in cancer and has received honoraria from Cell Signaling and Kineticos.

412 **References:**

413

414 1. E. D. Thompson, H. L. Enriquez, Y. X. Fu, V. H. Engelhard, Tumor masses support
415 naive T cell infiltration, activation, and differentiation into effectors. *J Exp Med* **207**,
416 1791-1804 (2010).
417 2. N. Prokhnevska *et al.*, CD8(+) T cell activation in cancer comprises an initial
418 activation phase in lymph nodes followed by effector differentiation within the
419 tumor. *Immunity* **56**, 107-124 e105 (2023).
420 3. A. R. Lim, W. K. Rathmell, J. C. Rathmell, The tumor microenvironment as a
421 metabolic barrier to effector T cells and immunotherapy. *Elife* **9**, (2020).
422 4. J. Wei, J. Raynor, T. L. Nguyen, H. Chi, Nutrient and Metabolic Sensing in T Cell
423 Responses. *Front Immunol* **8**, 247 (2017).
424 5. E. J. Wherry, M. Kurachi, Molecular and cellular insights into T cell exhaustion. *Nat*
425 *Rev Immunol* **15**, 486-499 (2015).
426 6. X. Lan, C. C. Zebley, B. Youngblood, Cellular and molecular waypoints along the
427 path of T cell exhaustion. *Sci Immunol* **8**, eadg3868 (2023).
428 7. M. W. Rudloff *et al.*, Hallmarks of CD8(+) T cell dysfunction are established within
429 hours of tumor antigen encounter before cell division. *Nat Immunol* **24**, 1527-1539
430 (2023).
431 8. N. Kedia-Mehta, D. K. Finlay, Competition for nutrients and its role in controlling
432 immune responses. *Nat Commun* **10**, 2123 (2019).
433 9. Y. Bian *et al.*, Cancer SLC43A2 alters T cell methionine metabolism and histone
434 methylation. *Nature* **585**, 277-282 (2020).
435 10. R. I. Klein Geltink, E. L. Pearce, The importance of methionine metabolism. *Elife*
436 **8**, (2019).
437 11. X. Yang *et al.*, MAT2A-Mediated S-Adenosylmethionine Level in CD4(+) T Cells
438 Regulates HIV-1 Latent Infection. *Front Immunol* **12**, 745784 (2021).
439 12. V. Papalazarou, O. D. K. Maddocks, Supply and demand: Cellular nutrient uptake
440 and exchange in cancer. *Mol Cell* **81**, 3731-3748 (2021).

13. P. Yu *et al.*, Priming of naive T cells inside tumors leads to eradication of established tumors. *Nat Immunol* **5**, 141-149 (2004).
14. D. S. Thommen, T. N. Schumacher, T Cell Dysfunction in Cancer. *Cancer Cell* **33**, 547-562 (2018).
15. Z. Zhang *et al.*, Pan-cancer landscape of T-cell exhaustion heterogeneity within the tumor microenvironment revealed a progressive roadmap of hierarchical dysfunction associated with prognosis and therapeutic efficacy. *EBioMedicine* **83**, 104207 (2022).
16. A. Kallies, D. Zehn, D. T. Utzschneider, Precursor exhausted T cells: key to successful immunotherapy? *Nat Rev Immunol* **20**, 128-136 (2020).
17. W. H. Hudson *et al.*, Proliferating Transitory T Cells with an Effector-like Transcriptional Signature Emerge from PD-1(+) Stem-like CD8(+) T Cells during Chronic Infection. *Immunity* **51**, 1043-1058 e1044 (2019).
18. D. T. Utzschneider *et al.*, Early precursor T cells establish and propagate T cell exhaustion in chronic infection. *Nat Immunol* **21**, 1256-1266 (2020).
19. F. Alfei *et al.*, TOX reinforces the phenotype and longevity of exhausted T cells in chronic viral infection. *Nature* **571**, 265-269 (2019).
20. N. Manolios, J. Papaemmanouil, D. J. Adams, The role of ion channels in T cell function and disease. *Front Immunol* **14**, 1238171 (2023).
21. Q. Feng *et al.*, Lactate increases stemness of CD8 + T cells to augment anti-tumor immunity. *Nat Commun* **13**, 4981 (2022).
22. G. T. Hart, K. A. Hogquist, S. C. Jameson, Kruppel-like factors in lymphocyte biology. *J Immunol* **188**, 521-526 (2012).
23. H. A. Abdelsamed *et al.*, Beta cell-specific CD8(+) T cells maintain stem cell memory-associated epigenetic programs during type 1 diabetes. *Nat Immunol* **21**, 578-587 (2020).
24. J. C. Beltra *et al.*, Stat5 opposes the transcription factor Tox and rewires exhausted CD8(+) T cells toward durable effector-like states during chronic antigen exposure. *Immunity* **56**, 2699-2718 e2611 (2023).
25. Q. Sun *et al.*, STAT3 regulates CD8+ T cell differentiation and functions in cancer and acute infection. *J Exp Med* **220**, (2023).
26. C. Zheng *et al.*, Transcriptomic profiles of neoantigen-reactive T cells in human gastrointestinal cancers. *Cancer Cell* **40**, 410-423 e417 (2022).
27. J. A. Belk, B. Daniel, A. T. Satpathy, Epigenetic regulation of T cell exhaustion. *Nat Immunol* **23**, 848-860 (2022).
28. E. J. Wherry *et al.*, Molecular signature of CD8+ T cell exhaustion during chronic viral infection. *Immunity* **27**, 670-684 (2007).
29. T. A. Doering *et al.*, Network analysis reveals centrally connected genes and pathways involved in CD8+ T cell exhaustion versus memory. *Immunity* **37**, 1130-1144 (2012).
30. M. Trebak, J. P. Kinet, Calcium signalling in T cells. *Nat Rev Immunol* **19**, 154-169 (2019).
31. P. G. Hogan, Calcium-NFAT transcriptional signalling in T cell activation and T cell exhaustion. *Cell Calcium* **63**, 66-69 (2017).
32. G. J. Martinez *et al.*, The transcription factor NFAT promotes exhaustion of activated CD8(+) T cells. *Immunity* **42**, 265-278 (2015).

487 33. M. A. Caudill *et al.*, Intracellular S-adenosylhomocysteine concentrations predict
488 global DNA hypomethylation in tissues of methyl-deficient cystathionine beta-
489 synthase heterozygous mice. *J Nutr* **131**, 2811-2818 (2001).
490 34. N. Zhang, Role of methionine on epigenetic modification of DNA methylation and
491 gene expression in animals. *Anim Nutr* **4**, 11-16 (2018).
492 35. J. W. Hwang, Y. Cho, G. U. Bae, S. N. Kim, Y. K. Kim, Protein arginine
493 methyltransferases: promising targets for cancer therapy. *Exp Mol Med* **53**, 788-
494 808 (2021).
495 36. A. A. Al-Hamashi, K. Diaz, R. Huang, Non-Histone Arginine Methylation by Protein
496 Arginine Methyltransferases. *Curr Protein Pept Sci* **21**, 699-712 (2020).
497 37. J. Lam, H. Wulff, The Lymphocyte Potassium Channels Kv1.3 and KCa3.1 as
498 Targets for Immunosuppression. *Drug Dev Res* **72**, 573-584 (2011).
499 38. R. K. Rader *et al.*, T cell activation is regulated by voltage-dependent and calcium-
500 activated potassium channels. *J Immunol* **156**, 1425-1430 (1996).
501 39. M. D. Cahalan, K. G. Chandy, The functional network of ion channels in T
502 lymphocytes. *Immunol Rev* **231**, 59-87 (2009).
503 40. S. K. Vodnala *et al.*, T cell stemness and dysfunction in tumors are triggered by a
504 common mechanism. *Science* **363**, (2019).
505 41. M. Bachmann *et al.*, Pharmacological targeting of the mitochondrial calcium-
506 dependent potassium channel KCa3.1 triggers cell death and reduces tumor
507 growth and metastasis in vivo. *Cell Death Dis* **13**, 1055 (2022).
508 42. H. Wulff *et al.*, Design of a potent and selective inhibitor of the intermediate-
509 conductance Ca2+-activated K+ channel, IKCa1: a potential immunosuppressant.
510 *Proc Natl Acad Sci U S A* **97**, 8151-8156 (2000).
511 43. J. C. Beltra *et al.*, Developmental Relationships of Four Exhausted CD8(+) T Cell
512 Subsets Reveals Underlying Transcriptional and Epigenetic Landscape Control
513 Mechanisms. *Immunity* **52**, 825-841 e828 (2020).
514 44. L. M. McLane, M. S. Abdel-Hakeem, E. J. Wherry, CD8 T Cell Exhaustion During
515 Chronic Viral Infection and Cancer. *Annu Rev Immunol* **37**, 457-495 (2019).
516 45. Q. Sun *et al.*, Immune checkpoint therapy for solid tumours: clinical dilemmas and
517 future trends. *Signal Transduct Target Ther* **8**, 320 (2023).
518 46. R. C. Sterner, R. M. Sterner, CAR-T cell therapy: current limitations and potential
519 strategies. *Blood Cancer J* **11**, 69 (2021).
520 47. F. Marofi *et al.*, CAR T cells in solid tumors: challenges and opportunities. *Stem*
521 *Cell Res Ther* **12**, 81 (2021).
522 48. H. Du *et al.*, Antitumor Responses in the Absence of Toxicity in Solid Tumors by
523 Targeting B7-H3 via Chimeric Antigen Receptor T Cells. *Cancer Cell* **35**, 221-237
524 e228 (2019).
525 49. N. E. Scharping *et al.*, The Tumor Microenvironment Represses T Cell
526 Mitochondrial Biogenesis to Drive Intratumoral T Cell Metabolic Insufficiency and
527 Dysfunction. *Immunity* **45**, 374-388 (2016).
528 50. F. Franco, A. Jaccard, P. Romero, Y. R. Yu, P. C. Ho, Metabolic and epigenetic
529 regulation of T-cell exhaustion. *Nat Metab* **2**, 1001-1012 (2020).
530 51. M. Shakiba *et al.*, TCR signal strength defines distinct mechanisms of T cell
531 dysfunction and cancer evasion. *J Exp Med* **219**, (2022).

52. A. Quintana, D. Griesemer, E. C. Schwarz, M. Hoth, Calcium-dependent activation of T-lymphocytes. *Pflugers Arch* **450**, 1-12 (2005).
53. B. T. Abe, D. S. Shin, E. Mocholi, F. Macian, NFAT1 supports tumor-induced anergy of CD4(+) T cells. *Cancer Res* **72**, 4642-4651 (2012).

Supplementary Materials References.

1. S. Zhao *et al.*, NKD2, a negative regulator of Wnt signaling, suppresses tumor growth and metastasis in osteosarcoma. *Oncogene* **34**, 5069-5079 (2015).
2. D. Haydar *et al.*, Cell-surface antigen profiling of pediatric brain tumors: B7-H3 is consistently expressed and can be targeted via local or systemic CAR T-cell delivery. *Neuro Oncol* **23**, 999-1011 (2021).
3. G. Sharma *et al.*, Analysis of 26 amino acids in human plasma by HPLC using AQC as derivatizing agent and its application in metabolic laboratory. *Amino Acids* **46**, 1253-1263 (2014).
4. B. Meszaros *et al.*, Recent breakthroughs in computational structural biology harnessing the power of sequences and structures. *Curr Opin Struct Biol* **80**, 102608 (2023).
5. C. H. Lee, R. MacKinnon, Activation mechanism of a human SK-calmodulin channel complex elucidated by cryo-EM structures. *Science* **360**, 508-513 (2018).
6. S. Jo, T. Kim, V. G. Iyer, W. Im, CHARMM-GUI: a web-based graphical user interface for CHARMM. *J Comput Chem* **29**, 1859-1865 (2008).
7. J. Lee *et al.*, CHARMM-GUI Input Generator for NAMD, GROMACS, AMBER, OpenMM, and CHARMM/OpenMM Simulations Using the CHARMM36 Additive Force Field. *J Chem Theory Comput* **12**, 405-413 (2016).
8. E. L. Wu *et al.*, CHARMM-GUI Membrane Builder toward realistic biological membrane simulations. *J Comput Chem* **35**, 1997-2004 (2014).
9. M. A. Lomize, I. D. Pogozheva, H. Joo, H. I. Mosberg, A. L. Lomize, OPM database and PPM web server: resources for positioning of proteins in membranes. *Nucleic Acids Res* **40**, D370-376 (2012).
10. W. L. Jorgensen, J. Chandrasekhar, J. D. Madura, R. W. Impey, M. L. Klein, Comparison of simple potential functions for simulating liquid water. *The Journal of Chemical Physics* **79**, 926-935 (1983).
11. D. A. Case *et al.*, AmberTools. *J Chem Inf Model* **63**, 6183-6191 (2023).
12. P. B. N, *Mathematics of Computation* **28**, 669-671 (1974).
13. in *Oeuvres complètes: Series 1,* A.-L. Cauchy, Ed. (Cambridge University Press, Cambridge, 2009), vol. 10, pp. 399-402.
14. S. E. Feller, Y. Zhang, R. W. Pastor, B. R. Brooks, Constant pressure molecular dynamics simulation: The Langevin piston method. *The Journal of Chemical Physics* **103**, 4613-4621 (1995).
15. J. Åqvist, P. Wennerström, M. Nervall, S. Bjelic, B. O. Brandsdal, Molecular dynamics simulations of water and biomolecules with a Monte Carlo constant pressure algorithm. *Chemical Physics Letters* **384**, 288-294 (2004).
16. J.-P. Ryckaert, G. Ciccotti, H. J. C. Berendsen, Numerical integration of the cartesian equations of motion of a system with constraints: molecular dynamics of n-alkanes. *Journal of Computational Physics* **23**, 327-341 (1977).

578 17. T. Darden, D. York, L. Pedersen, Particle mesh Ewald: An N·log(N) method for
579 Ewald sums in large systems. *The Journal of Chemical Physics* **98**, 10089-10092
580 (1993).
581 18. J. Huang *et al.*, CHARMM36m: an improved force field for folded and intrinsically
582 disordered proteins. *Nat Methods* **14**, 71-73 (2017).
583 19. R. B. Best *et al.*, Optimization of the additive CHARMM all-atom protein force field
584 targeting improved sampling of the backbone phi, psi and side-chain chi(1) and
585 chi(2) dihedral angles. *J Chem Theory Comput* **8**, 3257-3273 (2012).
586 20. W. Humphrey, A. Dalke, K. Schulten, VMD: visual molecular dynamics. *J Mol*
587 *Graph* **14**, 33-38, 27-38 (1996).
588 21. B. Langmead, S. L. Salzberg, Fast gapped-read alignment with Bowtie 2. *Nat*
589 *Methods* **9**, 357-359 (2012).
590 22. H. Li *et al.*, The Sequence Alignment/Map format and SAMtools. *Bioinformatics*
591 **25**, 2078-2079 (2009).
592 23. D. W. Barnett, E. K. Garrison, A. R. Quinlan, M. P. Stromberg, G. T. Marth,
593 BamTools: a C++ API and toolkit for analyzing and managing BAM files.
594 *Bioinformatics* **27**, 1691-1692 (2011).
595 24. P. A. Ewels *et al.*, The nf-core framework for community-curated bioinformatics
596 pipelines. *Nat Biotechnol* **38**, 276-278 (2020).
597 25. H. M. Amemiya, A. Kundaje, A. P. Boyle, The ENCODE Blacklist: Identification of
598 Problematic Regions of the Genome. *Sci Rep* **9**, 9354 (2019).
599 26. F. Ramirez *et al.*, deepTools2: a next generation web server for deep-sequencing
600 data analysis. *Nucleic Acids Res* **44**, W160-165 (2016).
601 27. Y. Zhang *et al.*, Model-based analysis of ChIP-Seq (MACS). *Genome Biol* **9**, R137
602 (2008).
603 28. A. R. Quinlan, I. M. Hall, BEDTools: a flexible suite of utilities for comparing
604 genomic features. *Bioinformatics* **26**, 841-842 (2010).
605 29. W. J. Kent, A. S. Zweig, G. Barber, A. S. Hinrichs, D. Karolchik, BigWig and
606 BigBed: enabling browsing of large distributed datasets. *Bioinformatics* **26**, 2204-
607 2207 (2010).
608 30. C. S. Ross-Innes *et al.*, Differential oestrogen receptor binding is associated with
609 clinical outcome in breast cancer. *Nature* **481**, 389-393 (2012).
610 31. Y. Chen, A. T. Lun, G. K. Smyth, From reads to genes to pathways: differential
611 expression analysis of RNA-Seq experiments using Rsubread and the edgeR
612 quasi-likelihood pipeline. *F1000Res* **5**, 1438 (2016).
613 32. G. Yu, L. G. Wang, Q. Y. He, ChIPseeker: an R/Bioconductor package for ChIP
614 peak annotation, comparison and visualization. *Bioinformatics* **31**, 2382-2383
615 (2015).
616 33. A. Subramanian *et al.*, Gene set enrichment analysis: a knowledge-based
617 approach for interpreting genome-wide expression profiles. *Proc Natl Acad Sci U*
618 *S A* **102**, 15545-15550 (2005).
619 34. G. Yu, L. G. Wang, Y. Han, Q. Y. He, clusterProfiler: an R package for comparing
620 biological themes among gene clusters. *OMICS* **16**, 284-287 (2012).
621 35. M. P. Meers, T. D. Bryson, J. G. Henikoff, S. Henikoff, Improved CUT&RUN
622 chromatin profiling tools. *Elife* **8**, (2019).

36. A. Dobin, T. R. Gingeras, Mapping RNA-seq Reads with STAR. *Curr Protoc Bioinformatics* **51**, 11 14 11-11 14 19 (2015).
37. B. Li, C. N. Dewey, RSEM: accurate transcript quantification from RNA-Seq data with or without a reference genome. *BMC Bioinformatics* **12**, 323 (2011).
38. M. I. Love, W. Huber, S. Anders, Moderated estimation of fold change and dispersion for RNA-seq data with DESeq2. *Genome Biol* **15**, 550 (2014).
39. D. Risso, J. Ngai, T. P. Speed, S. Dudoit, Normalization of RNA-seq data using factor analysis of control genes or samples. *Nat Biotechnol* **32**, 896-902 (2014).
40. A. Liberzon *et al.*, The Molecular Signatures Database (MSigDB) hallmark gene set collection. *Cell Syst* **1**, 417-425 (2015).
41. K. Yu *et al.*, High-Throughput Profiling of Proteome and Posttranslational Modifications by 16-Plex TMT Labeling and Mass Spectrometry. *Methods Mol Biol* **2228**, 205-224 (2021).
42. J. K. Eng *et al.*, A deeper look into Comet--implementation and features. *J Am Soc Mass Spectrom* **26**, 1865-1874 (2015).
43. X. Wang *et al.*, JUMP: a tag-based database search tool for peptide identification with high sensitivity and accuracy. *Mol Cell Proteomics* **13**, 3663-3673 (2014).
44. J. Peng, J. E. Elias, C. C. Thoreen, L. J. Licklider, S. P. Gygi, Evaluation of multidimensional chromatography coupled with tandem mass spectrometry (LC/LC-MS/MS) for large-scale protein analysis: the yeast proteome. *J Proteome Res* **2**, 43-50 (2003).
45. J. E. Elias, S. P. Gygi, Target-decoy search strategy for increased confidence in large-scale protein identifications by mass spectrometry. *Nat Methods* **4**, 207-214 (2007).
46. M. Niu *et al.*, Extensive Peptide Fractionation and y(1) Ion-Based Interference Detection Method for Enabling Accurate Quantification by Isobaric Labeling and Mass Spectrometry. *Anal Chem* **89**, 2956-2963 (2017).
47. B. Bai *et al.*, Deep Multilayer Brain Proteomics Identifies Molecular Networks in Alzheimer's Disease Progression. *Neuron* **105**, 975-991 e977 (2020).
48. G. K. Smyth, Linear models and empirical bayes methods for assessing differential expression in microarray experiments. *Stat Appl Genet Mol Biol* **3**, Article3 (2004).

Main Figure:

FIGURE 1

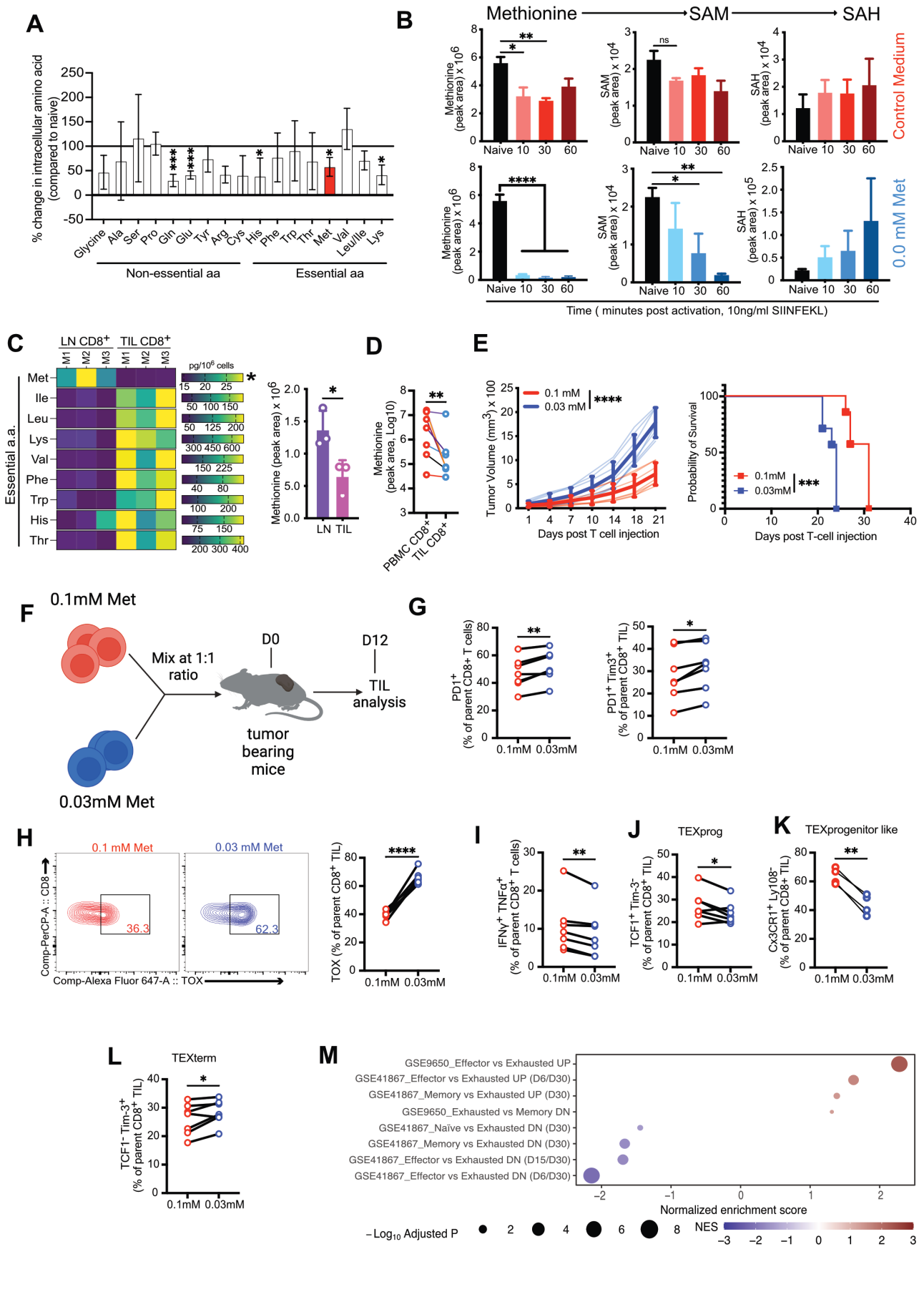
A
% change in intracellular amino acid (compared to naive)
Glycine Ala Ser Pro Gln Glu Tyr Arg Cys His Phe Trp Thr Met Val Leu/Ile Lys
Non-essential aa
Essential aa
B
Methionine → SAM → SAH
Control Medium
0.0 mM Met
Naive 10 30 60
Time (minutes post activation, 10ng/ml SIINFEKL)
C
LN CD8+
TIL CD8+
pg/10^6 cells
Essential a.a.
Met Ile Leu Lys Val Phe Trp His Thr
LN TIL
D
Methionine (peak area, Log10)
PBMC CD8+
TIL CD8+
E
0.1 mM
0.03 mM
Tumor Volume (mm3) x 100
Days post T cell injection
Probability of Survival
0.1mM
0.03mM
Days post T-cell injection
F
0.1mM Met
Mix at 1:1 ratio
D0
D12
TIL analysis
tumor bearing mice
0.03mM Met
G
PD1+ (% of parent CD8+ T cells)
PD1+ Tim3+ (% of parent CD8+ TIL)
0.1mM 0.03mM
H
0.1 mM Met
0.03 mM Met
36.3
62.3
Comp-PerCP-A :: CD8
Comp-Alexa Fluor 647-A :: TOX
TOX (% of parent CD8+ TIL)
I
IFNγ+ TNFα+ (% of parent CD8+ T cells)
J
TEXprog
TCF1+ Tim-3- (% of parent CD8+ TIL)
K
TEXprogenitor like
Cx3CR1+ Ly108- (% of parent CD8+ TIL)
L
TEXterm
TCF1- Tim-3+ (% of parent CD8+ TIL)
M
GSE9650_Effector vs Exhausted UP
GSE41867_Effector vs Exhausted UP (D6/D30)
GSE41867_Memory vs Exhausted UP (D30)
GSE9650_Exhausted vs Memory DN
GSE41867_Naïve vs Exhausted DN (D30)
GSE41867_Memory vs Exhausted DN (D30)
GSE41867_Effector vs Exhausted DN (D15/D30)
GSE41867_Effector vs Exhausted DN (D6/D30)
Normalized enrichment score
−Log10 Adjusted P
NES

662 **Figure 1: TCR-mediated, rapid methionine consumption governs anti-tumor effector**
663 **function. (A,B)** Quantification of intracellular amino acids 10 min (a), SAM and SAH up to 60
664 min (b) in OT-I T cells activated with 10 ng/ml SIINFEKL (n=3). **(C)** Quantification of essential
665 amino acids (left) and peak area of Met (right) in LN $CD8^+$ T cells and $CD8^+$ TIL, isolated at day
666 12 post tumor implantation (n=3). **(D)** Quantification of intracellular Met in $CD8^+$ PBMC and
667 $CD8^+$ TIL isolated from patient primary colorectal tumors (n= 8). **(E)** Tumor growth (left) and
668 survival (right) of B16-OVA tumors in $Rag1^{-/-}$ mice after transfer of 24 hr activated OT-I T cells
669 initially activated in 0.1 or 0.03 mM Met with 2.5ng/ml SIINFEKL for 30 min, followed by
670 restoration of 0.03 mM to 0.1 mM Met (n=5). **(F)** Schematic of experimental design. OT-I $CD8^+$
671 T cells with different congenic markers were initially activated in 0.1 mM or 0.03 mM Met for 30
672 min with replenishment of Met in 0.03 mM to 0.1 mM Met for 24 hrs, transferred into B16-OVA
673 tumor bearing $Rag1^{-/-}$ mouse at a 1:1 ratio and analyzed day 12 post T cell transfer. **(G)** Frequency
674 of $PD1^+$ and $PD1^+Tim\text{-}3^+$ cells of OT-I $CD8^+$ TIL, initially activated in 0.1 mM and 0.03 mM Met
675 and assessed at D12 post injection (n=7). **(H-I)** Contour plot and frequency of TOX^+ cells (h) and
676 frequency of $IFN\gamma^+TNF\alpha^+$ (i) of OT-I $CD8^+$ TIL as in G (n=7). **(J-L)** Frequency of (j) $TCF1^+Tim\text{-}$
677 3^- TEXprog, $CX3CR1^+Ly108^+$ TEXprogenitor-like (k) and, $TCF1^-Tim\text{-}3^+$ TEXterm (l) cells in
678 OT-I $CD8^+$ T cells initially activated as in E (n=7, n=4). **(M)** T cell exhaustion gene sets in GSEA
679 analysis of RNA-Seq of OT-I $CD8^+$ TIL as in E n=4. Data are mean±s.e.m. Unpaired two-tailed
680 Student's t-test (A-D), two-way ANOVA (E-left), Mantel-Cox log rank test (E--right) and paired
681 two-tailed Student's t-test (G-L) *$P < 0.05$, **$P < 0.01$, ***$P < 0.001$, ****$P < 0.0001$.

FIGURE 2

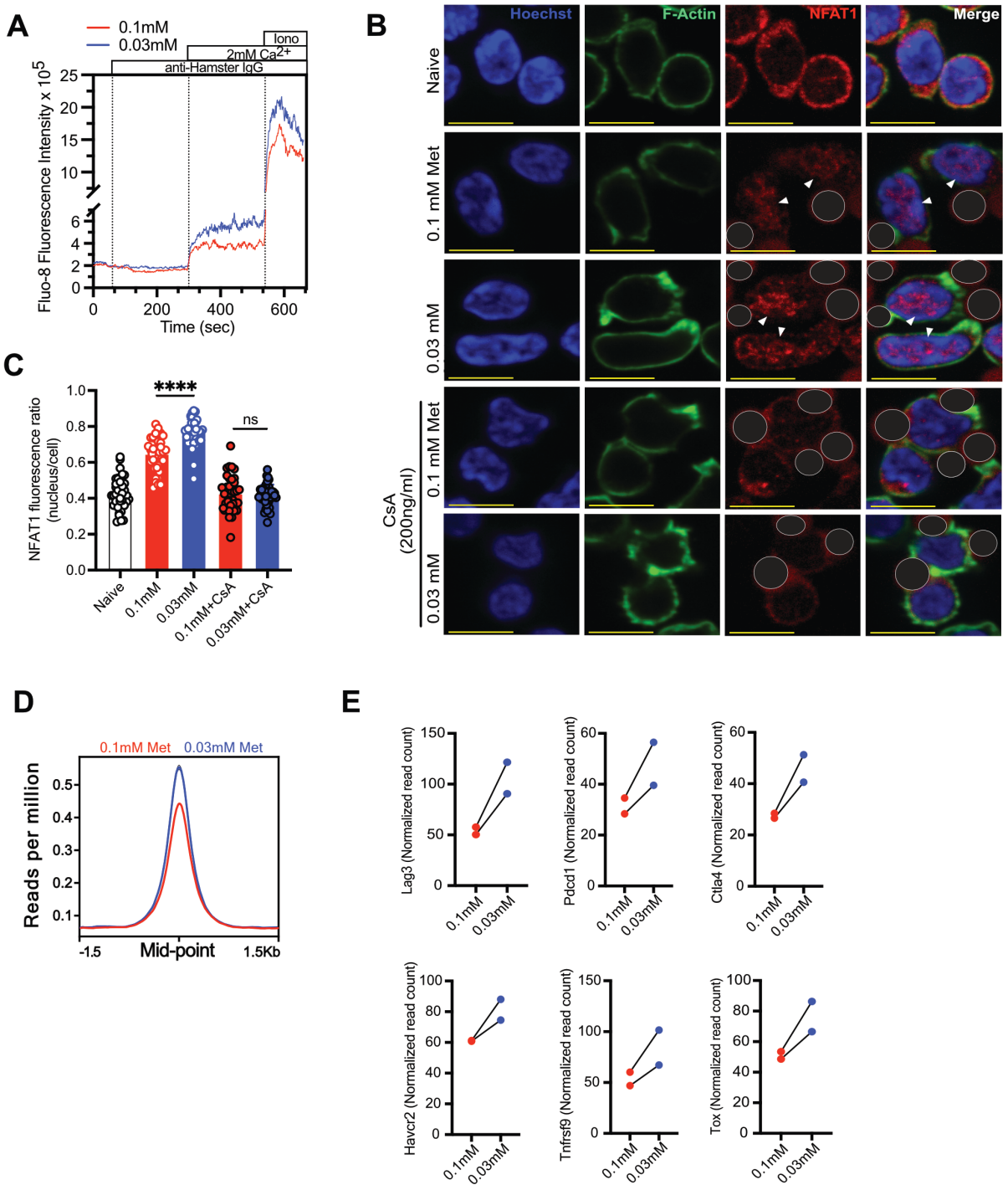

682

683 **Figure 2: Extracellular methionine availability regulates NFAT1 activation and T cell**
684 **exhaustion. (A)** Fluo-8 AM analysis of Ca^{2+} flux in $CD8^{+}$ T cells activated with anti-CD3 and
685 anti-CD28 by anti-hamster IgG crosslinking in either 0.1 mM or 0.03 mM Met containing Ca^{2+}

686 Ringer solution with addition of 2 mM Ca^{2+} to measure Ca^{2+} influx. Representative of 2
687 experiments. **(B, C)** Representative images of T cells, cultured with or without anti-CD3/28
688 dynabeads (dark grey masked), in 0.1 mM and 0.03 mM Met, with or without cyclosporin-A
689 treatment for 30 min, stained with NFAT1 (red, marked), Hoechst (blue) and Phalloidin (green)
690 (b). Quantification of NFAT1 intensity as nuclear to cell ratio (c) (See Fig. S4A for unmasked
691 figure). Scale bar=10μm. (Each circle represents one cell, n=40 cells). **(D, E)** Histogram of NFAT1
692 binding signals (d), read count per million reads normalized to background) and quantification of
693 known NFAT1-binding regions of *Lag3, Pdcd1, Havcr2, Ctla4* and *Tnfrsf9 and Tox* (e, normalized
694 read count (see differential binding analysis)) in T cells initially activated in 0.1 or 0.03 mM Met
695 for 30 min and assessed 24 hrs post activation (n=2). Data are mean±s.e.m. Unpaired two-tailed
696 Student's t-test (C, D). *P < 0.05, **P < 0.01, ***P < 0.001, ****P < 0.0001.

FIGURE 3

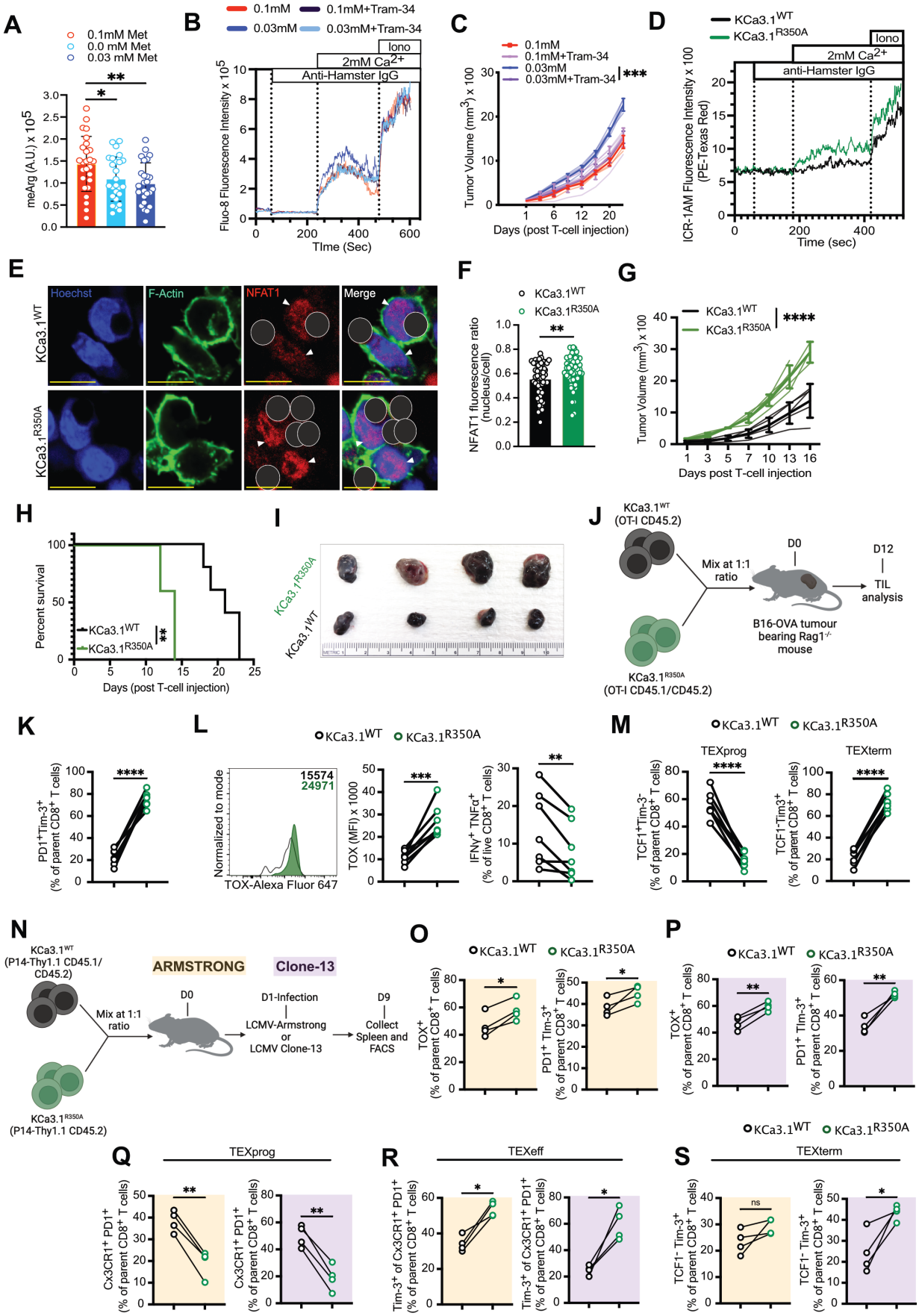
A
0.1mM Met
0.0 mM Met
0.03 mM Met
meArg (A.U.) x 10^5
B
0.1mM
0.1mM+Tram-34
0.03mM
0.03mM+Tram-34
Iono
2mM Ca2+
Anti-Hamster IgG
Fluo-8 Fluorescence Intensity x 10^5
TIme (Sec)
C
0.1mM
0.1mM+Tram-34
0.03mM
0.03mM+Tram-34
Tumor Volume (mm3) x 100
Days (post T-cell injection)
D
KCa3.1WT
KCa3.1R350A
Iono
2mM Ca2+
anti-Hamster IgG
ICR-1AM Fluorescence Intensity x 100 (PE-Texas Red)
Time (sec)
E
Hoechst
F-Actin
NFAT1
Merge
KCa3.1WT
KCa3.1R350A
F
KCa3.1WT
KCa3.1R350A
NFAT1 fluorescence ratio (nucleus/cell)
G
KCa3.1WT
KCa3.1R350A
Tumor Volume (mm3) x 100
Days post T-cell injection
H
Percent survival
KCa3.1WT
KCa3.1R350A
Days (post T-cell injection)
I
KCa3.1R350A
KCa3.1WT
J
KCa3.1WT (OT-I CD45.2)
Mix at 1:1 ratio
D0
D12
TIL analysis
B16-OVA tumour bearing Rag1-/-
KCa3.1R350A (OT-I CD45.1/CD45.2)
K
PD1+Tim-3+ (% of parent CD8+ T cells)
L
KCa3.1WT
KCa3.1R350A
Normalized to mode
15574
24971
TOX-Alexa Fluor 647
TOX (MFI) x 1000
IFNγ+ TNFα+ (% of live CD8+ T cells)
M
KCa3.1WT
KCa3.1R350A
TEXprog
TEXterm
TCF1+Tim-3- (% of parent CD8+ T cells)
TCF1+Tim3+ (% of parent CD8+ T cells)
N
KCa3.1WT (P14-Thy1.1 CD45.1/ CD45.2)
ARMSTRONG
Clone-13
Mix at 1:1 ratio
D0
D1-Infection
LCMV-Armstrong or LCMV Clone-13
D9
Collect Spleen and FACS
KCa3.1R350A (P14-Thy1.1 CD45.2)
O
KCa3.1WT
KCa3.1R350A
TOX+ (% of parent CD8+ T cells)
PD1+ Tim-3+ (% of parent CD8+ T cells)
P
KCa3.1WT
KCa3.1R350A
TOX+ (% of parent CD8+ T cells)
PD1+ Tim-3+ (% of parent CD8+ T cells)
Q
TEXprog
Cx3CR1+ PD1+ (% of parent CD8+ T cells)
R
TEXeff
Tim-3+ of Cx3CR1+ PD1+ (% of parent CD8+ T cells)
S
KCa3.1WT
KCa3.1R350A
TEXterm
TCF1- Tim-3+ (% of parent CD8+ T cells)
ns

697

698 **Figure 3. KCa3.1 arginine 350 methylation regulates NFAT1-activity upon T cell activation.**
699 **(A)** Quantification of methyl-arginine in $CD8^+$ T cells activated with anti-CD3/28 dynabeads in
700 0.1, 0.0, or 0.03 mM Met for 30 min (each circle represents one cell. n= 25 cells). **(B)** Fluo-8 AM
701 analysis of Ca^{2+} flux in $CD8^+$ T cells activated with anti-CD3 and anti-CD28 by anti-hamster IgG
702 crosslinking in either 0.1 mM or 0.03 mM Met containing Ca^{2+}-free Ringer solution treated either
703 with DMSO or 1μM TRAM-34. **(C)** Tumor growth of B16-OVA tumors in $Rag1^{-/-}$ mouse after
704 transfer of OT-I $CD8^+$ T cells activated in 0.1 mM or 0.03 mM Met with either DMSO or 1 μM
705 TRAM-34 for 30 min and cultured for 24 hrs (n=5). **(D)** ICR-1 AM analysis of Ca^{2+} flux in
706 $KCa3.1^{WT}$ and $KCa3.1^{R350A}$ T cells activated with anti-CD3 and anti-CD28 by anti-hamster IgG
707 crosslinking in Ca^{2+}-free Ringer solution. **(E, F)** Representative image (e) and quantification of
708 NFAT1intensity as nuclear to cell ratio (f) in $KCa3.1^{WT}$ and $KCa3.1^{R350A}$ OT-I T cells activated
709 for 30 min with anti-CD3/28 dynabeads (dark grey masked) (See Fig. S6C for unmasked figure),
710 scale bar=10 μm (each circle represents one cell, n=40 cells). **(G, H)** Tumor growth (g) and
711 survival (h) of B16-OVA tumor-bearing $RAG^{-/-}$ mice after transfer of $KCa3.1^{WT}$ and $KCa3.1^{R350A}$
712 OT-I T cells (n=5). **(I)** B16-OVA tumors harvested at D12 post transfer of $KCa3.1^{WT}$ and
713 $KCa3.1^{R350A}$ OT-I T cells (n=4). **(J)** Schematic of experimental design to assess congenically
714 distinct $KCa3.1^{WT}$ and $KCa3.1^{R350A}$ OT-I T cells, mixed at a 1:1 ratio and transferred into B16-
715 OVA tumor bearing $Rag1^{-/-}$ mice and analyzed day 12 post T cell transfer. **(K-L)** Frequency of
716 $Tim\text{-}3^+PD1^+$ (k), histogram and quantification of TOX MFI, and frequency of $IFN\gamma^+TNF\alpha^+$ (l) in
717 $KCa3.1^{WT}$ and $KCa3.1^{R350A}$ OT-I TIL at D12 post T-cell transfer as in J (n=7). **(M)** Frequency of
718 $TCF1^+Tim\text{-}3^-$ TEXprog and $TCF1^-Tim\text{-}3^+$ TEXterm in $KCa3.1^{WT}$ and $KCa3.1^{R350A}$ OT-I TIL at
719 D12 post T-cell transfer as in J (n=7). **(N)** Schematic of experimental design to assess congenically
720 distinct $KCa3.1^{WT}$ and $KCa3.1^{R350A}$ Thy1.1 P14 T cells, mixed at a 1:1 ratio, transferred into WT
721 mice, and infected with either LCMV-Armstrong or LCMV-Clone-13. Spleens were analyzed at
722 D9 post infection. **(O, P)** Frequency of Tox^+ and $PD1^+Tim\text{-}3^+$ in $KCa3.1^{WT}$ and $KCa3.1^{R350A}$ P14
723 $CD8^+$ T cells from spleens at D9 post infection with either LCMV-Armstrong (o) or LCMV-Clone-
724 13 (p) (n=4). **(Q-S)** Frequency of $CX3CR1^+PD1^+$ TEXprog (q), $Tim\text{-}3^+$ of $CX3CR1^+PD1^+$
725 TEXeffector-like (r) and $TCF1^-Tim\text{-}3^+$ TEXterm (s) in $KCa3.1^{WT}$ and $KCa3.1^{R350A}$ P14 $CD8^+$ T
726 cells from spleens at D9 post infection as in N (n=4). Data are mean±s.e.m. Unpaired two-tailed
727 Student's t-test (A, F), 2-way ANOVA (C, G), Mantel-Cox test (H) and paired two-tailed Student's
728 t-test (K-M, O-S). *P < 0.05, **P < 0.01, ***P < 0.001, ****P < 0.0001.

FIGURE 4

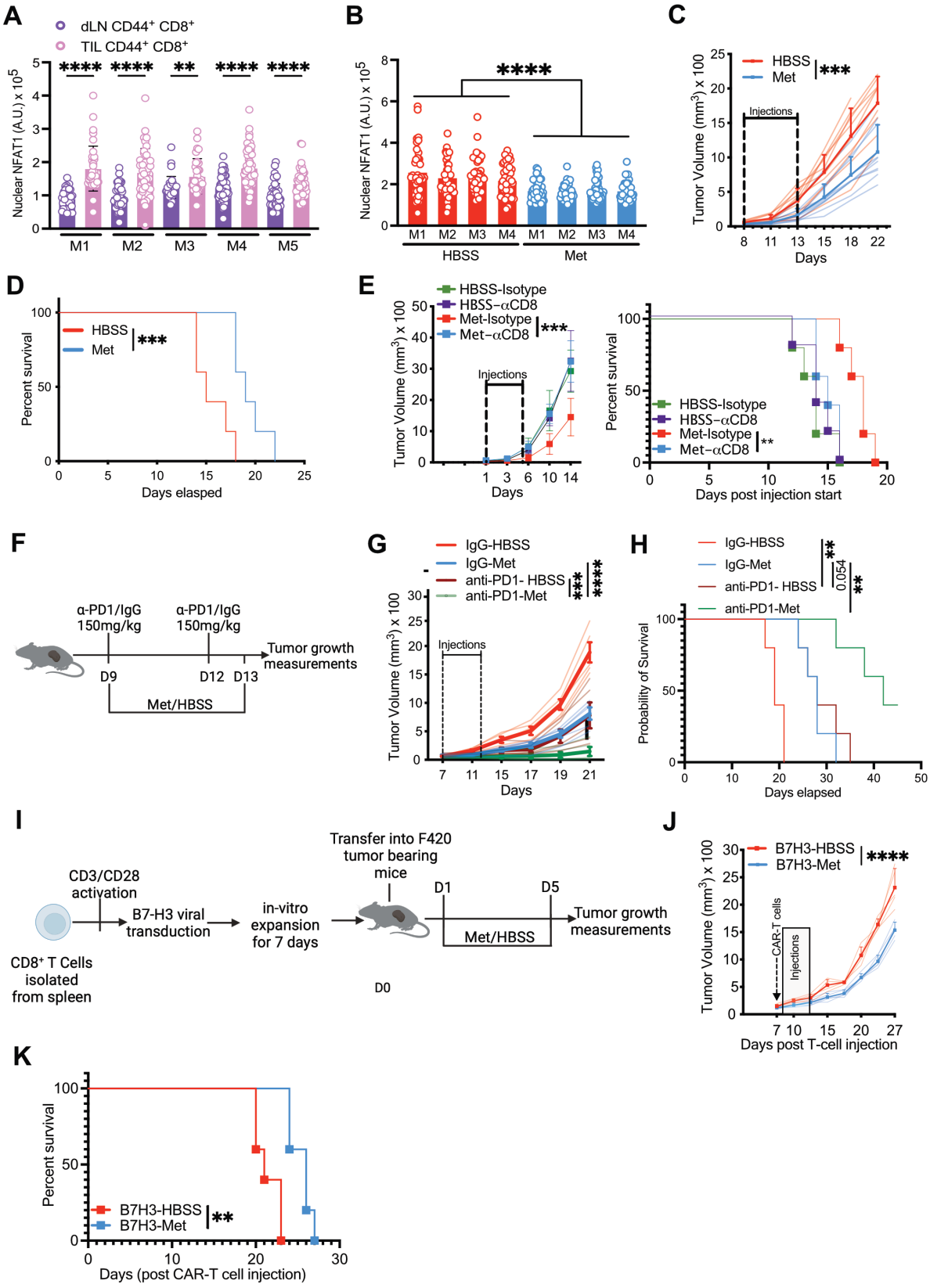
A
dLN CD44+ CD8+
TIL CD44+ CD8+
Nuclear NFAT1 (A.U.) x 10^5
M1
M2
M3
M4
M5
B
Nuclear NFAT1 (A.U.) x 10^5
HBSS
Met
C
HBSS
Met
Injections
Tumor Volume (mm^3) x 100
Days
D
HBSS
Met
Percent survival
Days elasped
E
HBSS-Isotype
HBSS-αCD8
Met-Isotype
Met-αCD8
Injections
Tumor Volume (mm^3) x 100
Days
Percent survival
Days post injection start
F
α-PD1/IgG 150mg/kg
α-PD1/IgG 150mg/kg
Tumor growth measurements
D9
D12
D13
Met/HBSS
G
IgG-HBSS
IgG-Met
anti-PD1- HBSS
anti-PD1-Met
Injections
Tumor Volume (mm^3) x 100
Days
H
IgG-HBSS
IgG-Met
anti-PD1- HBSS
anti-PD1-Met
0.054
Probability of Survival
Days elapsed
I
CD3/CD28 activation
B7-H3 viral transduction
in-vitro expansion for 7 days
Transfer into F420 tumor bearing mice
D1
D5
Tumor growth measurements
Met/HBSS
CD8+ T Cells isolated from spleen
D0
J
B7H3-HBSS
B7H3-Met
CAR-T cells
Injections
Tumor Volume (mm^3) x 100
Days post T-cell injection
K
B7H3-HBSS
B7H3-Met
Percent survival
Days (post CAR-T cell injection)

730 **Figure 4. Acute methionine supplementation promotes CD8$^+$ T cell-mediated tumor control.**
731 **(A)** Nuclear NFAT1 quantification in CD44$^+$CD8$^+$ T cells isolated from B16 tumors and respective
732 dLNs at D9 post implantation (each circle represents one cell, n=40 cells, n=5). **(B)** Quantification
733 of nuclear NFAT1 in CD44$^+$ CD8$^+$ T cells isolated from B16 tumors, after 5 days of peri-tumoral
734 supplementation per day of 50 µl HBSS or 61 µM Met (each circle represents one cell, n=40 cells,
735 n=4). **(C, D)** Tumor growth (c) and survival (d) of B16 tumor-bearing WT mice, supplemented
736 either with HBSS or 61 µM Met peri-tumorally for five days as in B (n=10). **(E)** B16 tumor growth
737 (left) and survival (right) of WT mice, treated intraperitoneally with IgG isotype or anti-CD8
738 antibody at D-1 and D3 and treated peri-tumorally with HBSS or Met from D7-D12 as in B (n=5,
739 representative of two experiments). **(F)** Schematic design to assess tumor growth with anti-PD1
740 treatment and with either HBSS or Met supplementation. **(G, H)** Tumour growth (g) and survival
741 (h) of MC38 tumor-bearing WT mice, treated either with anti-PD1 or IgG-isotype and
742 supplemented with HBSS or Met peri-tumorally for five days as in B (n=5, representative of two
743 experiments). **(I)** Schematic of experimental design to assess the effect of HBSS or Met
744 supplementation on CAR-T cell therapy in mouse solid tumors. **(J, K)** Tumor growth (j) and
745 survival (k) of F420 tumor-bearing Rag1$^{-/-}$ mice injected with B7-H3 CAR T-cells at D0 and peri-
746 tumorally treated with HBSS or Met from D1-D6 as in B (n=5). Data are mean±s.e.m. Unpaired
747 two-tailed Student's t-test (A), 2-way ANOVA (C, E-left, G and J), and Mantel-Cox log rank test
748 (D, E-right, H and K). Statistical analysis of (B) is described in methods. *P < 0.05, **P < 0.01,
749 ***P < 0.001, ****P < 0.0001.s
750
751
752
753
754
755 **SUPPLEMENTARY FIGURES**

Supplementary Fig. 1

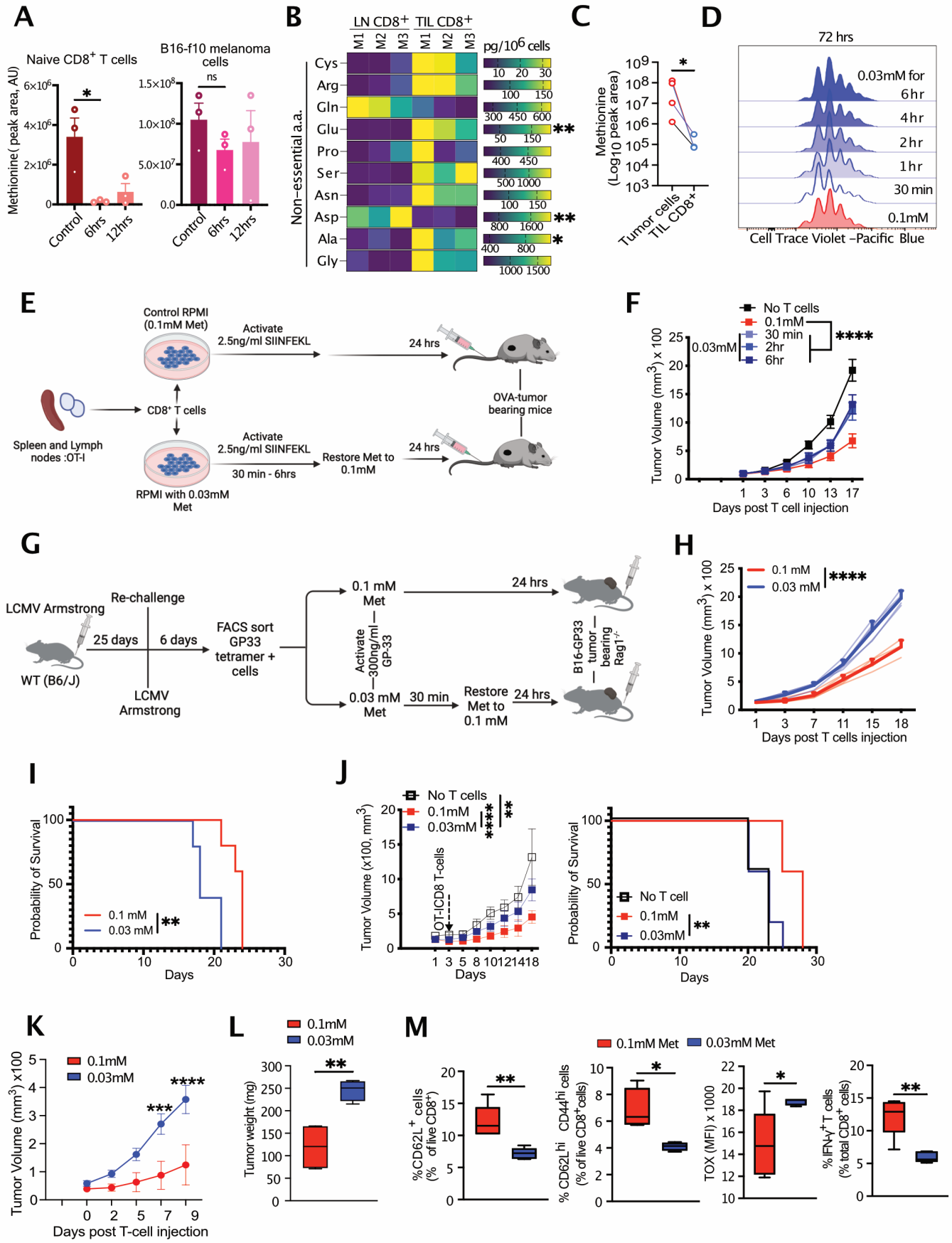

757 **Supplementary Figure 1: Met availability during TCR engagement determines anti-tumor T cell**
758 **function. (A)** Quantification of intracellular Met in $CD8^+$ T cells and B16 cells at 0, 6, and 12 hrs of
759 co-culture (n=3). **(B)** Quantification of intracellular non-essential amino acids from LN $CD8^+$ and
760 $CD8^+$ TIL, isolated at D12 post implantation of B16 tumors (n=3). **(C)** Quantification of intracellular
761 Met from tumor cells and $CD8^+$ TIL isolated from patient primary colorectal tumors (n=4). **(D)** T
762 cell proliferation via cell-trace violet staining of OT-I $CD8^+$ T cells activated in either 0.1 mM Met
763 or 0.03 mM Met for the indicated times before restoration to 0.1 mM Met in 0.03 mM Met
764 conditions, analyzed 72 hrs post activation (n=3). Representative of 3 samples per group. **(E)**
765 Schematic design for OT-I T cell activation initially in 0.1 or 0.03 mM Met, followed by restoration
766 of Met to 0.1 mM for 24 hrs before injection into B16-OVA tumor bearing mice. **(F)** Tumor growth
767 of B16-OVA in $Rag1^{-/-}$ treated with OT-I $CD8^+$ T cells activated as described in (E) for 30 min-6hrs
768 (n=5). **(G)** Schematic experimental design for generation of LCMV-GP33 specific memory T cells,
769 which were then activated as in described in (E) before injection into B16-OVA tumor-bearing
770 $Rag1^{-/-}$ mice. **(H, I)** Tumor growth (h) and survival (i) of B16-OVA tumors treated as described in
771 (G) (n=5). **(J)** Tumor growth and survival of B16-OVA tumor bearing WT mice treated with or
772 without OT-I $CD8^+$ T cells activated in 0.1 or 0.03 mM Met for 30 min before restoring Met to 0.1
773 mM in 0.03 mM Met for 24 hrs, as described in (E) (n=5). **(K)** Tumor growth of B16-OVA tumor
774 bearing $Rag1^{-/-}$ mice injected with OT-I T cells as in (E) (n=5). **(L, M)** Tumor weight (l) and
775 frequency of $CD62L^+$, Tcm ($CD62L^{hi}$ $CD44^{hi}$), IFN-γ^+, and TOX expression (MFI) (m) in OT-I $CD8^+$ TIL
776 isolated from B16-OVA tumor bearing $Rag1^{-/-}$ mice at D9 post-injection with OT-I T cells activated
777 as in (E) (n=5). Data are mean±s.e.m. Unpaired two-tailed Student's t-test (A, B, C, L and M), two-
778 way ANOVA (F and H) and Mantel-Cox test (I and J-right). *P < 0.05, **P < 0.01, ****P < 0.0001
779

780

Supplementary Fig. 2

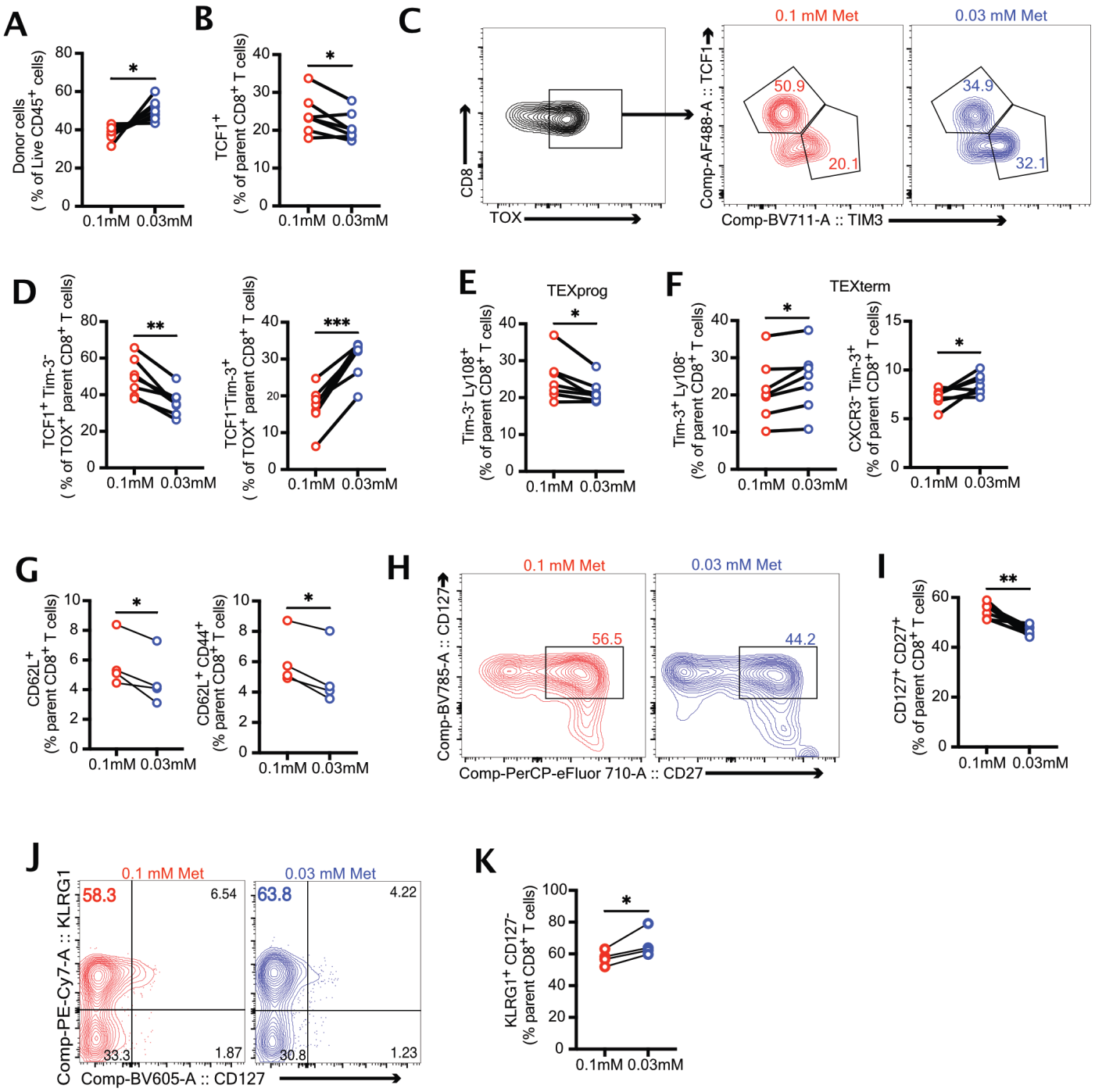

781

782 **Supplementary Figure 2: Met limitation promotes T cell exhaustion and hampers memory**

783 **generation. (A)** Frequencies of T cells isolated from B16-OVA tumors at D12 post transfer of OT-

784 I T cells activated as in Fig. S1E (n=7). **(B)** Expression of TCF1^{+} on OT-I CD8^{+} T cells at D12 post
785 transfer of OT-I T cells, activated as in Fig. S1E (n=7). **(C, D)** Representative contour plot (c) and
786 quantification (d) of TCF1 and Tim-3 expressing cells from TOX^{+} CD8^{+} TIL from OT-I CD8^{+} T cells
787 isolated at D12 post transfer of OT-I T cells activated as in Fig. S1E into B16-OVA tumor-bearing
788 Rag1$^{-/-}$ mice (n=7). **(E-G)** Frequency of Tim-3^{-}Ly108^{+} TEXprog (e), Tim-3^{+}Ly108^{-} , CXCR3^{-}Tim-3^{+}
789 TEXterm (f), CD62L^{+} T memory and CD62L^{+}CD44^{+} T central memory cells (g) in OT-I TIL as in (A)
790 (n=7 (f), n=4 (g)). **(H-J)** Representative contour plot and quantification of CD127^{+}CD27^{+} memory
791 cells (h, i) and KLRG1^{+}CD127^{-} terminal effector cells (j) in OT-I CD8^{+} TIL isolated at D12 post of
792 cells activated as in Fig. S1E into B16-OVA tumor-bearing Rag1$^{-/-}$ mice (n=4). Data are mean±s.e.m
793 with statistical analyses performed using paired two-tailed Student's t-test (*P < 0.05, **P < 0.01,
794 ***P < 0.001).
795
796
797
798
799
800
801
802
803
804
805
806
807
808
809

Supplementary Fig. 3

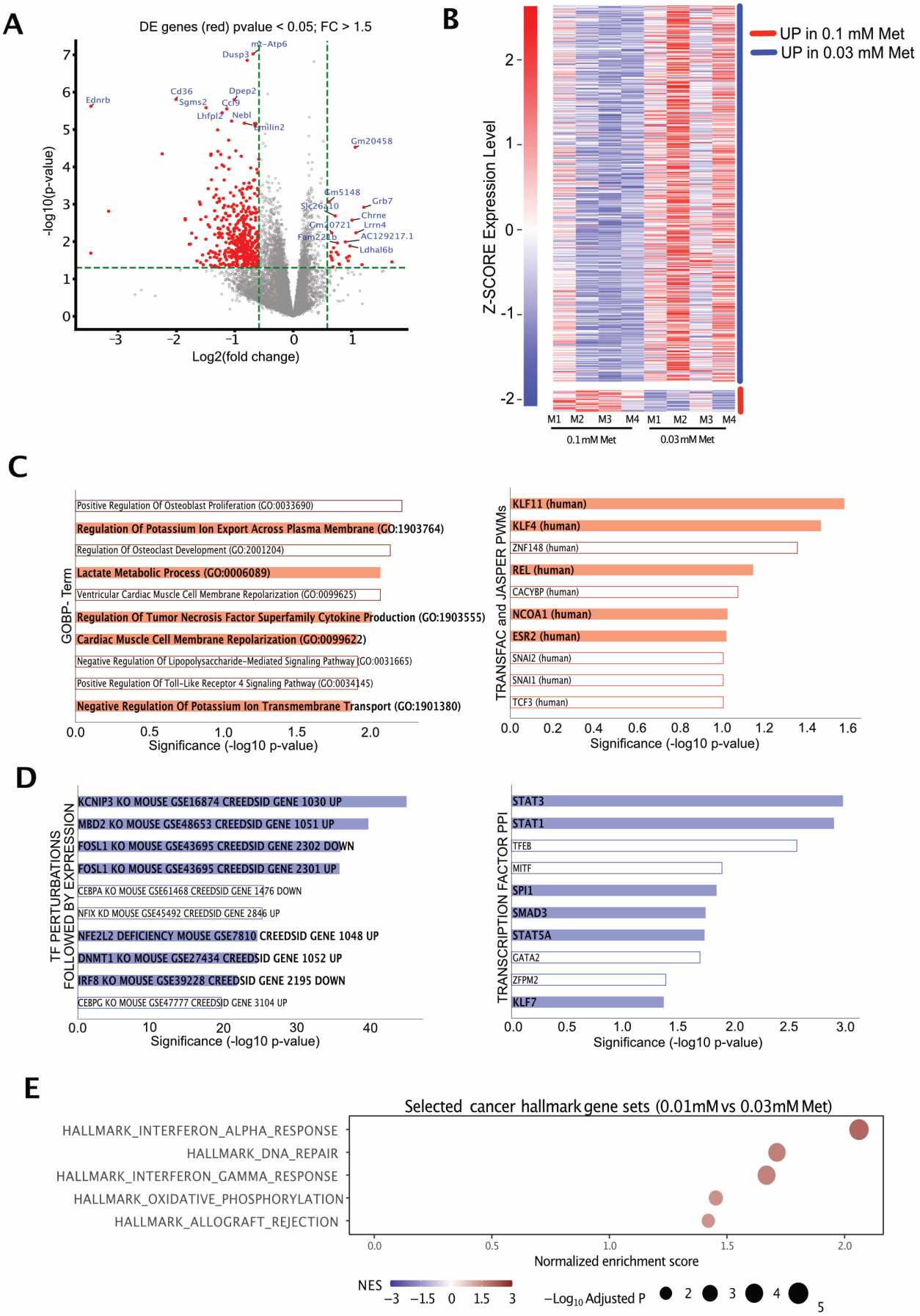

813 **Supplementary Figure 3: RNA-Seq analysis shows enrichment of exhaustion signature in low**
814 **Met. (A)** Volcano plot and top ten differentially expressed genes (red) (0.1 mM vs 0.03 mM,
815 $p<0.05$, FC>1.5) from OT-I $CD8^+$ TIL isolated from mice injected with OT-I T cells, initially activated
816 in 0.1 mM Met or 0.03 mM Met (as in Fig. S1E), at day 12 post injection into B16-OVA tumor-
817 bearing mice (n=4). **(B)** Heatmap of DE genes, which shows either increased expression in cells
818 initially activated in 0.03 mM Met or 0.1 mM Met, from the RNAseq in (A) (n=4). **(C)** Over-
819 representation analysis of DE genes with higher expression in TIL initially activated in 0.1 mM
820 Met, showing enrichment of biological processes and transcription factors associated with T cell
821 effector function and regulation. **(D)** Over-representation analysis of DE genes with higher
822 expression in TIL initially activated in 0.03 mM Met, showing enrichment of gene sets and
823 transcription factors associated with promotion and maintenance of the exhausted T cell state.
824 **(E)** GSEA analysis of hallmark genesets as analyzed from RNA-Seq of OT-I TIL initially activated in
825 0.1 or 0.03 mM Met, isolated from B16-OVA tumors at D12 post transfer (n=4). RNA-Seq statistics
826 were applied as described in methods.
827

Supplementary Fig. 4

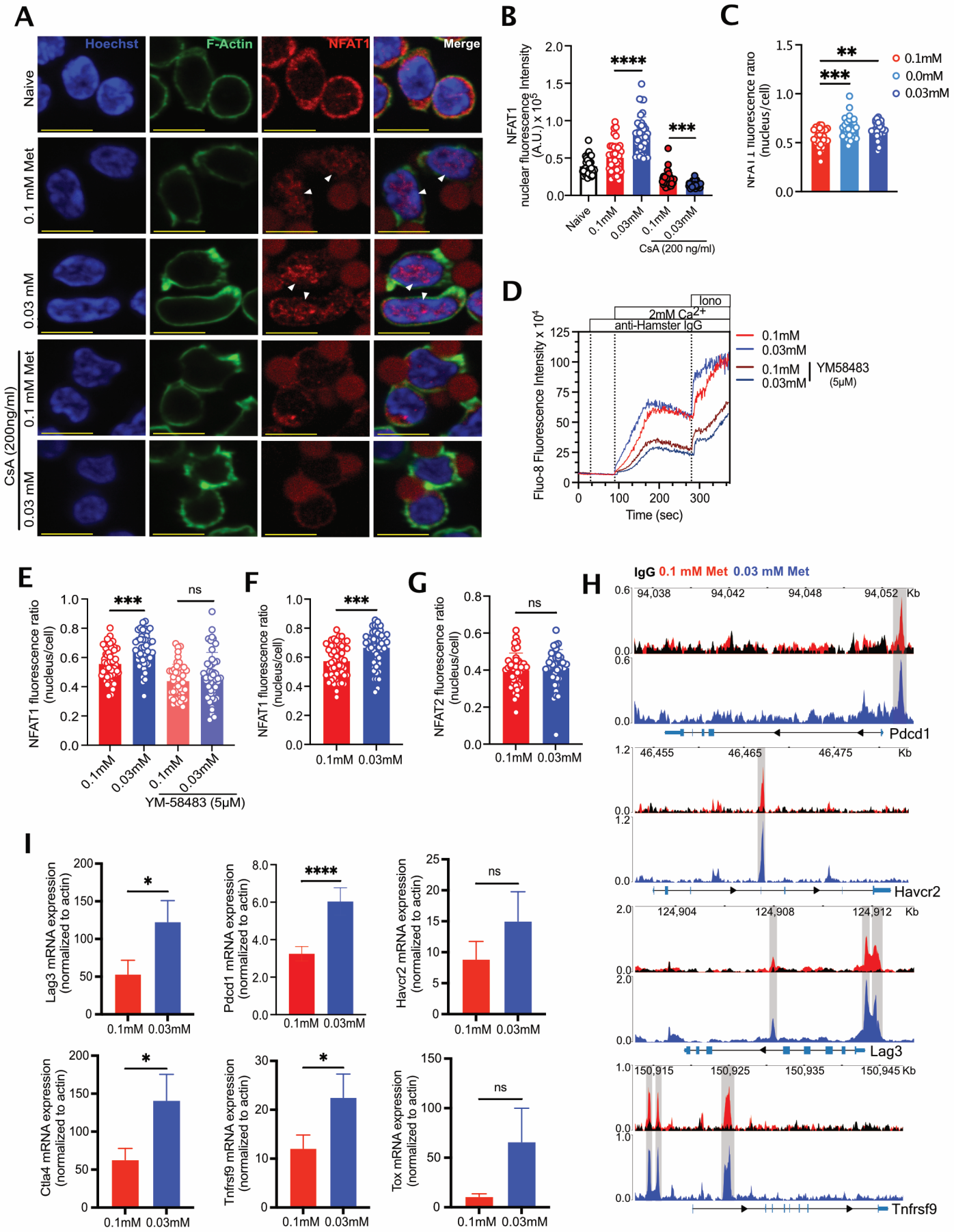

829 **Supplementary Fig. 4: Met limitation results in increased TCR-mediated NFAT1 activation.**
830 **(A)** Un-edited image of Figure. 2B showing the unmasked, Red CD3/38 dynabeads which are
831 masked grey in the main figure to highlight NFAT1 staining. **(B)** Quantification of nuclear NFAT1
832 from the experiment shown in Figure 2B. **(C)** NFAT1 intensity quantification (nuclear to cell ratio)
833 of $CD8^+$ T cells activated in either 0.1 mM, 0.00 mM or 0.03 mM Met for 30 min with anti CD3/28
834 dynabeads and stained for NFAT1 (each circle represents one cell, n=40 cells). **(D)** Fluo-8 AM
835 analysis of Ca^{2+} flux in $CD8^+$ T cells activated with anti-CD3 and anti-CD28 and anti-hamster IgG
836 crosslinking in either 0.1 mM or 0.03 mM Met containing Ca^{2+}-free Ringer solution treated with
837 DMSO or 5μM YM58483. **(E)** NFAT1 intensity quantification (nuclear to cell ratio) of $CD8^+$ T cells
838 activated for 30 min by CD3/28 dynabeads in either 0.1 mM or 0.03 mM Met in the presence of
839 DMSO or 5μM YM58483 (n=40 cells). **(F)** NFAT1 quantification (nuclear to cell ratio) of previously
840 activated OT-I T cells, treated with anti-CD3/28 dynabeads for 30 min. T cells were initially
841 activated with 2.5ng/ml SIINFEKL for 24 hrs in control medium and rested with 10 ng/ml mIL-7
842 for 48 hrs (each circle represents one cell, n=40). **(G)** NFAT2 quantification (nuclear to cell ratio)
843 of $CD8^+$ T cells, activated in 0.1 mM or 0.03 mM Met for 30 min with anti-CD3/28 dynabeads
844 (each circle represents one cell, n=40 cells). **(H)** NFAT1 Cut&Run tracks at *Pdcd1, Havcr2, Lag3,*
845 *and Tnfrsf9* locus. The gray highlights the peaks showing increased NFAT1 binding (n=2). **(I)**
846 Normalized RNA expression quantified by quantitative-PCR performed 24 hrs post activation of
847 OT-I $CD8^+$ T cells activated with 2.5 ng/ml SIINFEKL in 0.1 mM or 0.03 mM Met for 30 min followed
848 by 0.1 mM (n=6). Data are mean±s.e.m. Unpaired two-tailed Student's t-test (B, C, E, F, G) and
849 one-tailed Student's t-test (I). *P < 0.05, **P < 0.01, ***P < 0.001, ****P < 0.0001.
850

Supplementary Fig. 5

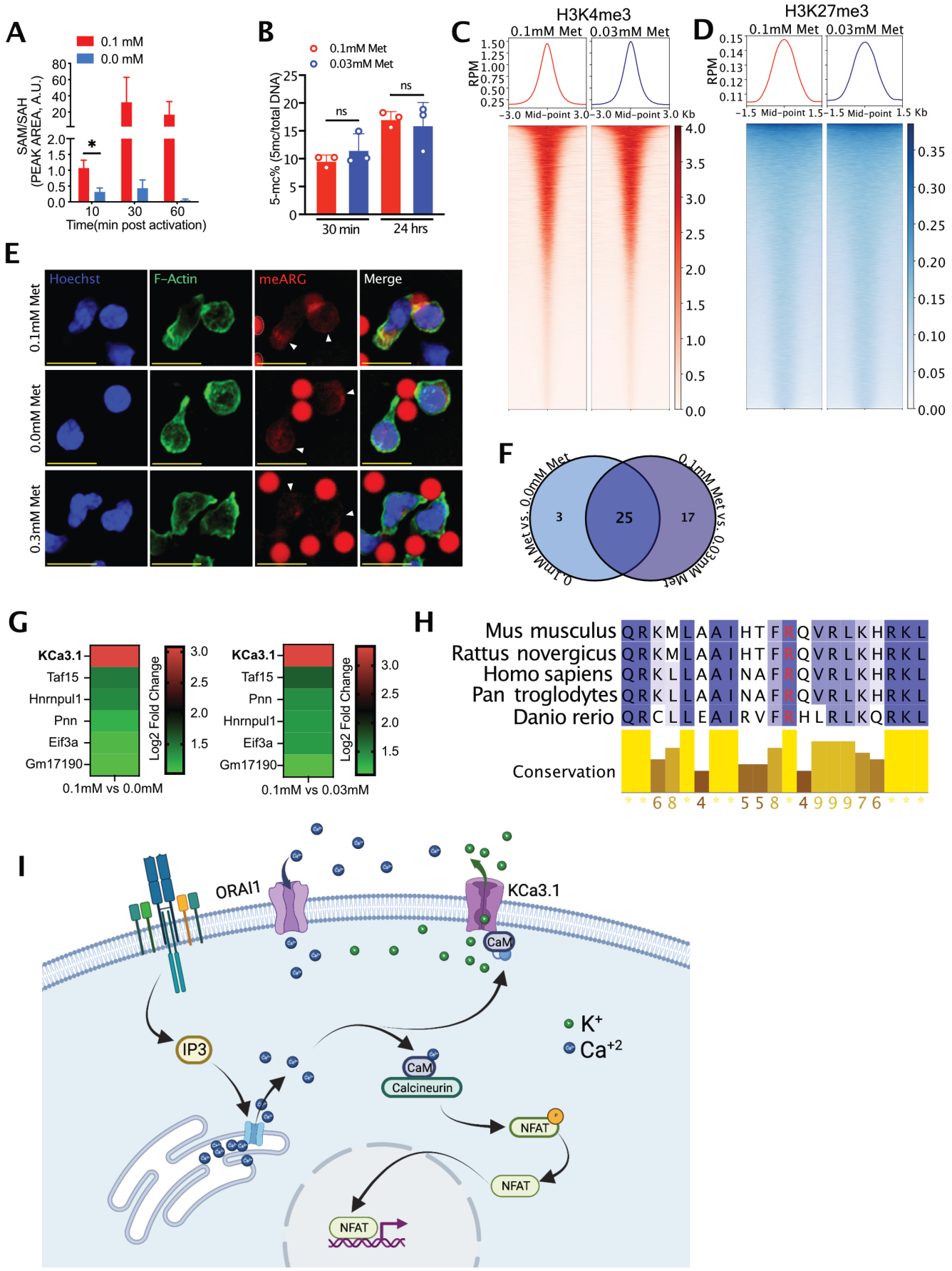

851

852 **Supplementary Fig. 5: Initial Met limitation results in reduced arginine methylation but not**
853 **DNA or histone methylation. (A)** Methylation potential (SAM/SAH) of 10 ng/ml SIINFEKL
854 activated OT-I T cells in 0.1 mM or 0.0 mM Met, at 10, 30 and 60 min (n=3). **(B)** % 5-methylytosine
855 (%5-mc) of OT-I $CD8^+$ T cells activated with 2.5 ng/ml SIINFEKL in 0.1 mM or 0.03 mM Met for 30
856 min, then 0.1 mM Met for 24 hr (n=3). **(C, D)** Histograms (top) and heat-map (bottom) of
857 H3K4me3 (c) and H3K27me3 (d) CUT&RUN reads (read count per million, normalized to
858 background) in OT-I $CD8^+$ T cells activated initially in 0.1 mM or 0.03 mM Met, with restoration
859 to 0.1 mM after 30 min and processed at 24 hrs post activation (n=3). **(E)** Representative images
860 of $CD8^+$ T cells activated with anti-CD3/28 dynabeads (circled bright red) in 0.1, 0.0, and 0.03 mM
861 Met for 30 min, stained with methyl-arginine (red, marked), Hoechst (blue), and Phalloidin
862 (green) (scale bar=10 μm) **(F)** Venn diagram of enriched methyl-arginine proteins at 30 min post
863 activation of T cells in 0.1 mM vs 0.0 mM or 0.1 mM vs 0.03 mM Met, as identified by TMT-MS.
864 **(G)** Heat-map (Log_2 fold change) of TMT-MS identified proteins ($p<0.05$) with enriched methyl-
865 arginine in T cells activated in 0.1 mM vs 0.0mM or 0.03 mM Met by IgG crosslinking with anti-
866 CD3 for 30 min (n=3). **(H)** Conserved arginine (highlighted red) in KCa3.1 as analyzed by protein-
867 BLAST in multiple species and visualized using Jalview. **(I)** Schematic pathway of TCR mediated
868 KCa3.1 activation and function. Data are mean±s.e.m. Unpaired one-tailed Student's t-test (A) or
869 unpaired two-tailed Student's t-test (B).
870

Supplementary Fig. 6

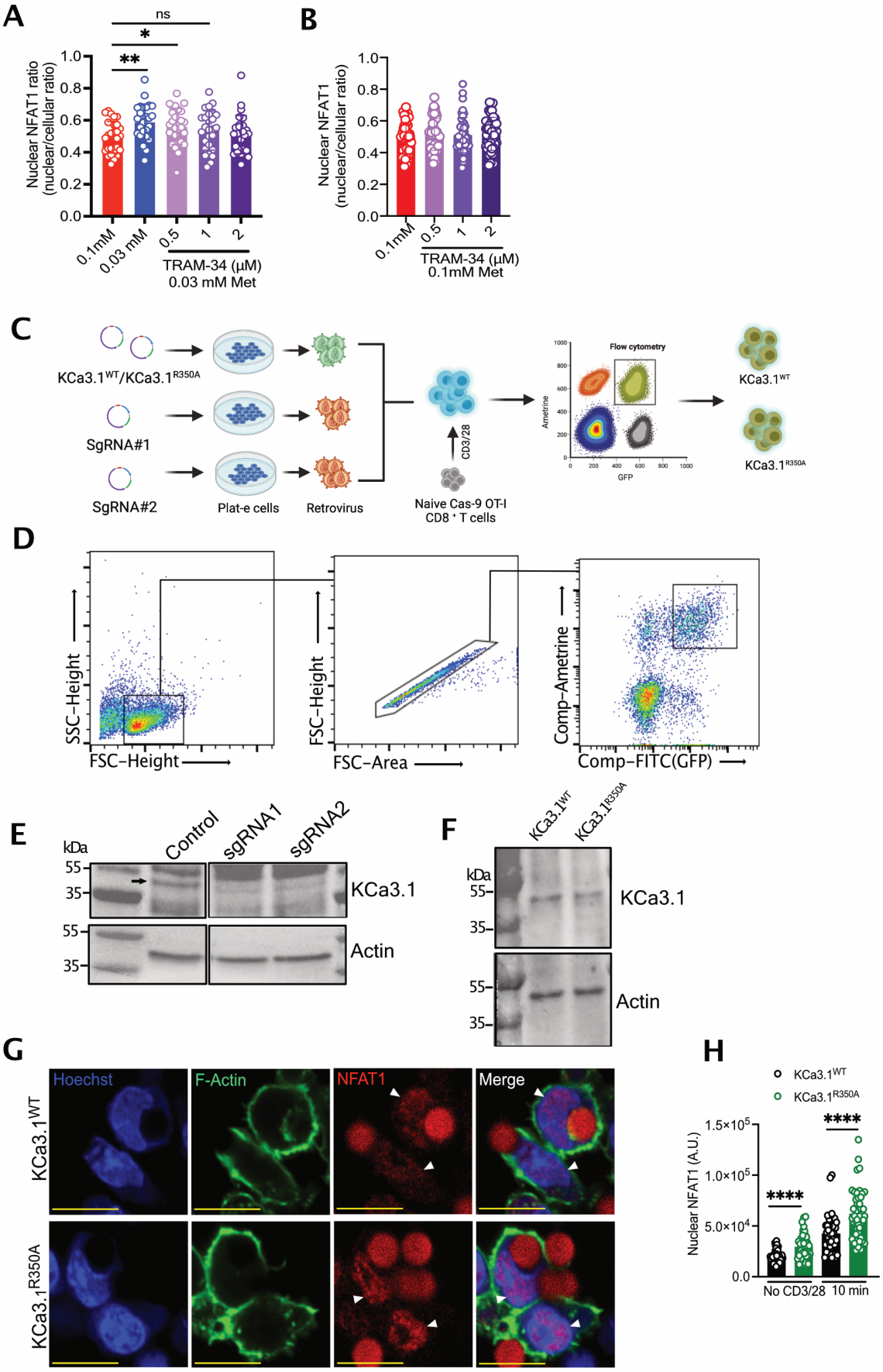

915 **Supplementary Fig. 6: KCa3.1 R350 methylation regulates NFAT1 activation. (A, B)** NFAT1
916 quantification (nuclear to cell ratio) in OT-I $CD8^+$ T cells activated for 30 min with anti CD3/28
917 dynabeads in 0.03 mM Met (a) or 0.1 mM Met (b) in the presence of 0.5, 1 or 2 μM TRAM-34
918 (each circle represents one cell, n=45). **(C)** Schematic of experimental design of endogenous
919 KCa3.1 knockdown with expression of $KCa3.1^{WT}$ and $KCa3.1^{R350A}$ in Cas9-OT-I or $P14^+$ $CD8^+$ T cells.
920 **(D)** Sorting strategy for *in vitro*-generated $KCa3.1^{WT}$ and $KCa3.1^{R350A}$ T cells; gate shows the cells
921 that express WT or R350A KCa3.1 with endogenous KCa3.1 knockdown. **(E)** Immunoblot showing
922 knockdown of KCa3.1 with sgRNA1 and sgRNA2, compared to control. **(F)** Immunoblot of KCa3.1
923 expression in $KCa3.1^{WT}$- and $KCa3.1^{R350A}$-expressing $CD8^+$ T cells. **(G)** Un-edited image of Figure.
924 3E showing the unmasked CD3/38 dynabeads which are masked grey in the main figure to
925 highlight NFAT1 staining. F. Nuclear NFAT1quantification of $KCa3.1^{WT}$ and $KCa3.1^{R350A}$, either
926 control (no Dynabeads) or activated with anti-CD3/28 Dynabeads for 10 min (each circle
927 represents one cell, n=45 cells). Data are mean±s.e.m. Unpaired two-tailed Student's t-test. *P <
928 0.05, **P < 0.01, ****P < 0.0001.

Supplementary Fig. 7

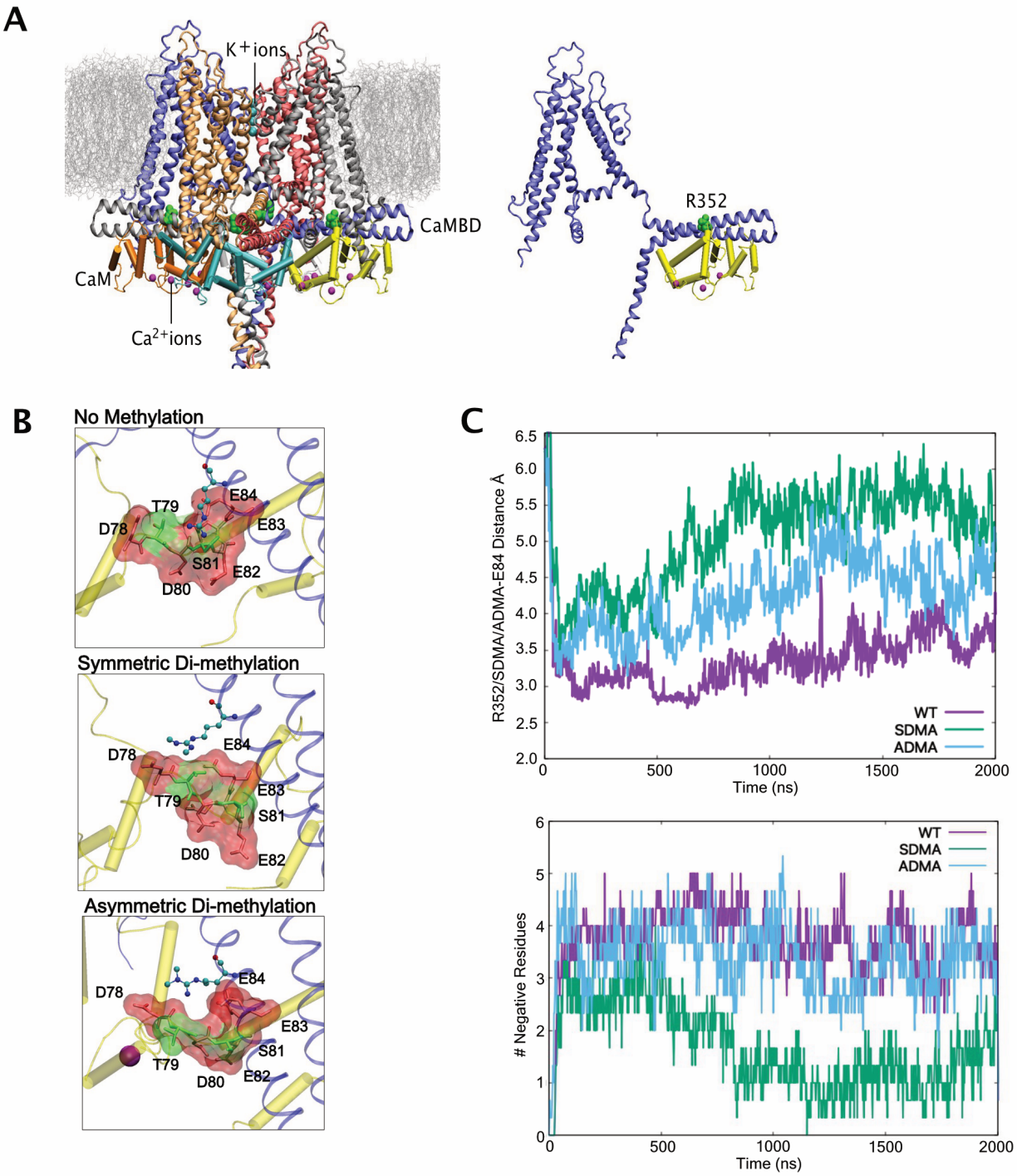

929

930 **Supplementary Fig. 7: huKCa3.1 R352 methylation weakens KCa3.1-Calmodulin interaction *in-***

931 ***silico*. (A)** Tetrameric assembly of human KCa3.1-Calmodulin complex within the membrane

932 (left). KCa3.1 is represented as ribbons and calmodulin quartet as cartoon with interacting Ca^{2+}

933 ions as purple spheres. K^+ ions are represented as cyan spheres. KCa3.1 monomer (blue) is shown
934 in complex with calmodulin (yellow) along with demethylated arginine-352 in green (right). **(B)**
935 Interaction of KCa3.1 monomer (blue cartoon) with calmodulin (yellow cartoon) as un-
936 methylated (top), SDMA (middle) and ADMA (bottom). The Calmodulin-binding pocket is
937 represented as surface with interacting amino acids as sticks (negatively charged-red, polar
938 residue-green) and R352 as ball and sticks; introduction of hydrophobic methyl group (middle
939 and bottom) weakens the interactions between calmodulin and KCa3.1 monomer. **(C)** MD
940 simulations analysis: Analysis of variations of distance of salt bridge between calmodulin E84 and
941 demethylated R352 (WT), SDMA R352 and ADMA R352 over the course of simulation time (top).
942 Illustration of total count of negatively charged residues within a 4Å radius of all four
943 R352/SDMA/ADMA of huKCa3.1 the course of simulation time (bottom) (averaged across all four
944 monomers, three MD trials).
945
946
947

Supplementary Fig. 8

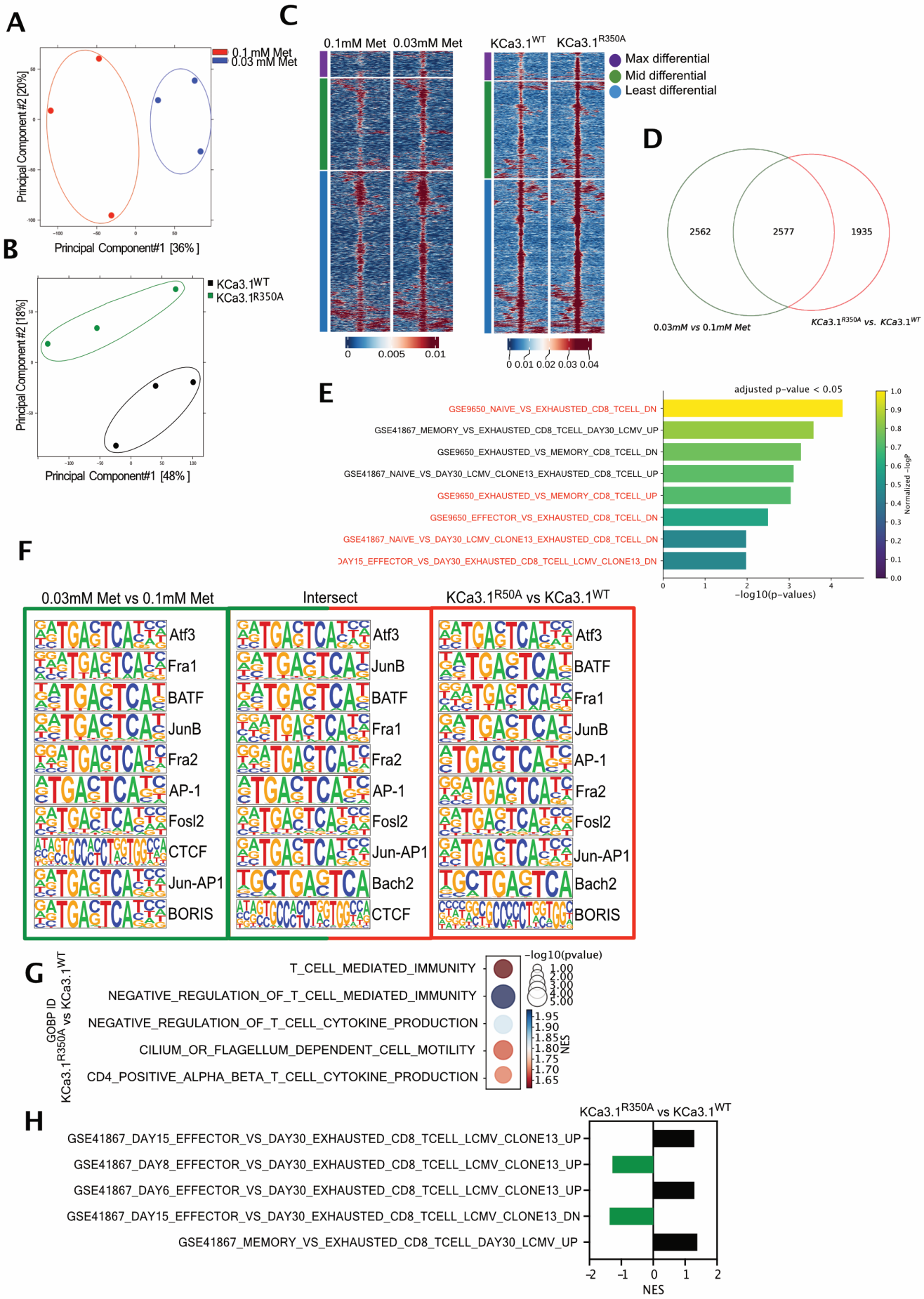

949 **Supplementary Fig. 8: ATAC-Seq analysis of KCa3.1 R350A similar exhaustion T cell signature as**
950 **of initial Met limitation. (A,B)** PCA analysis of ATAC-Seq of OT-I T cells, activated with 2.5ng/ml
951 SIINFEKL in 0.1 mM and 0.03 mM Met and cultured in 0.1 mM Met for 24 hrs (a), or KCa3.1^{WT}-
952 and KCa3.1^{R350A}- activated with 2.5 ng/ml SIINFEKL for 24 hrs (b). n=3. **(C)** Chromatin accessibility
953 heatmap of of T cells initially activated in 0.1 or 0.03 mM Met (left) or expressing activated
954 KCa3.1^{WT} or KCa3.1^{R350A} (right) with each row representing peaks ($p<0.05$ and log2 fold-change
955 >1.5) displayed over the span of 2kb window with peak as center (grouped from least to max
956 differential region), analyzed 24 hrs post activation with 2.5ng/ml SIINFEKL (n=3). **(D)** Common
957 differentially accessible regions (DAR) ($p<0.05$, fold change>1.5) between ATAC-Seq of OT-I cells
958 expressing KCa3.1^{WT} or KCa3.1^{R350A}, or OT-I cells initially activated in 0.1 mM or 0.03 mM Met as
959 in (A,B) **(E)** Over-representation analysis of the common DAR from (d) showing the top 8 gene
960 sets associated with exhaustion and activation. **(F)** Top 10 motifs analyzed by HOMER in ATAC-
961 Seq DAR's from OT-I CD8+ T cells initially activated in 0.03 mM Met vs 0.1 mM Met (left) or
962 expressing KCa3.1^{R350A} vs KCa3.1^{WT} and activated as (b) (middle), and from the common DAR's
963 from (d). **(G)** GOBP terms associated with negative regulation of T cells enriched in OT-I T cells
964 expressing KCa3.1^{R350A} vs KCa3.1^{WT} (activated at b) GSEA analysis of promoter reads from ATAC-
965 Seq post 24 hrs of activation (n=3). **(H)** T cell exhaustion gene sets in GSEA analysis of differential
966 accessible promoter reads from ATAC-Seq of OT-I T cells expressing KCa3.1^{WT} or KCa3.1^{R350A},
967 activated with 2.5 ng/ml SIINFEKL for 24 hrs (n=3).
968

Supplementary Fig. 9

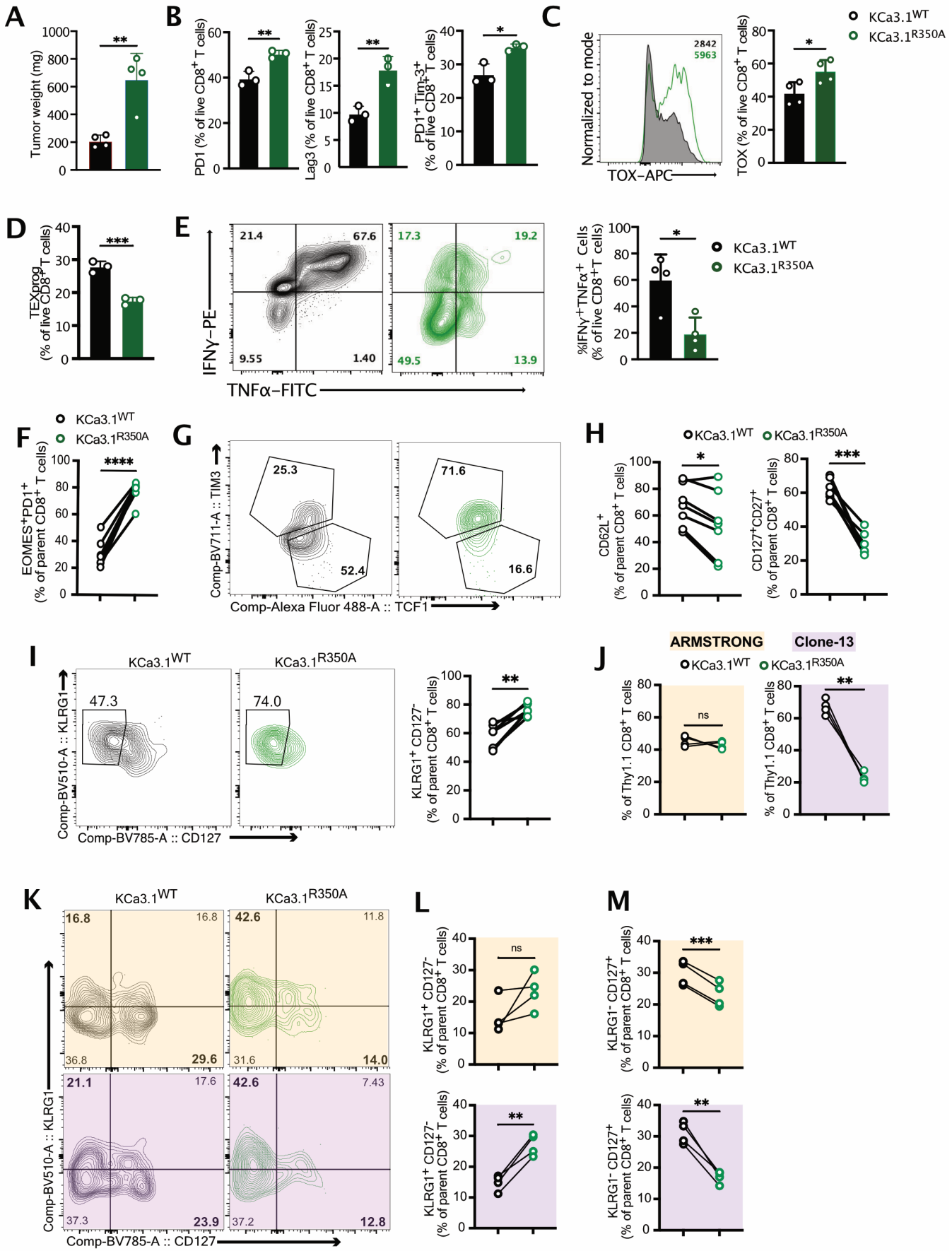

969

970 **Supplementary Fig. 9: Ablation of KCa3.1 R350 methylation promotes T cell exhaustion *in-vivo*.**
971 **(A)** Tumor weight of B16-OVA tumors isolated at D12 post transfer of OT-I T cells expressing
972 KCa3.1^{WT} or KCa3.1^{R350A} (n=4). **(B)** Surface expression of PD1^{+}, Lag3^{+} and PD1^{+}Tim-3^{+} in CD8^{+} TIL
973 isolated at D12 post transfer into B16-OVA tumor-bearing mice of OT-I T cells expressing
974 KCa3.1^{WT} or KCa3.1^{R350A} (n=4). **(C)** Representative histogram of TOX expression and quantification
975 in CD8^{+} TIL isolated at D12 post transfer of OT-I T cell expressing KCa3.1^{WT} or KCa3.1^{R350A} as (b)
976 (n=4). **(D)** Representative contour plot (left) and quantification of IFNγ^{+}TNFα^{+} (right) in OT-I T cells
977 expressing KCa3.1^{WT} or KCa3.1^{R350A} at D12 post transfer as (b) (n=4). **(F, G)** Expression of
978 EOMES^{+}PD1^{+} (f) and representative contour plot of expression of TCF1 and Tim-3 (g) on
979 congenically marked OT-I T cells expressing KCa3.1^{WT} or KCa3.1^{R350A}, mixed and transferred at a
980 ratio of 1:1. TIL were isolated from B16-OVA tumors at D12 post T cell transfer (n=7). **(H, I)**
981 Expression of memory markers CD62L and CD127^{+}CD27^{+} (h), representative contour plot and
982 quantification of KLRG1^{+}CD127^{-} terminal effector cells (i) on congenically marked OT-I T cells
983 expressing KCa3.1^{WT} or KCa3.1^{R350A}, as in (F), isolated at D12 post transfer into B16-OVA tumor-
984 bearing mice (n=7). **(J)** Frequency of KCa3.1^{WT}- and KCa3.1^{R350A} -expressing P14 T cells in spleens,
985 D9 post infection with either LCMV-Armstrong or LCMV-Clone-13 (n=4). **(K-M)** Representative
986 contour plot (k) and quantification of KLRG1^{+}CD127^{-} terminal effector cells (l) and KLRG1^{-}CD127^{+}
987 memory precursor cells (m) in spleens of animals injected with congenically marked P14 T cells
988 expressing KCa3.1^{WT} or KCa3.1^{R350A}, mixed 1:1, and infected with either LCMV-Armstrong or
989 LCMV-Clone-13. Analysis on d9 post infection (n=4). Data are mean±s.e.m. Unpaired two-tailed
990 Student's t-test (A-D) and paired two-tailed Student's t-test (F-M). *P < 0.05, **P < 0.01, ***P <
991 0.001, ****P < 0.0001.
992
993
994
995
996

Supplementary Fig. 10

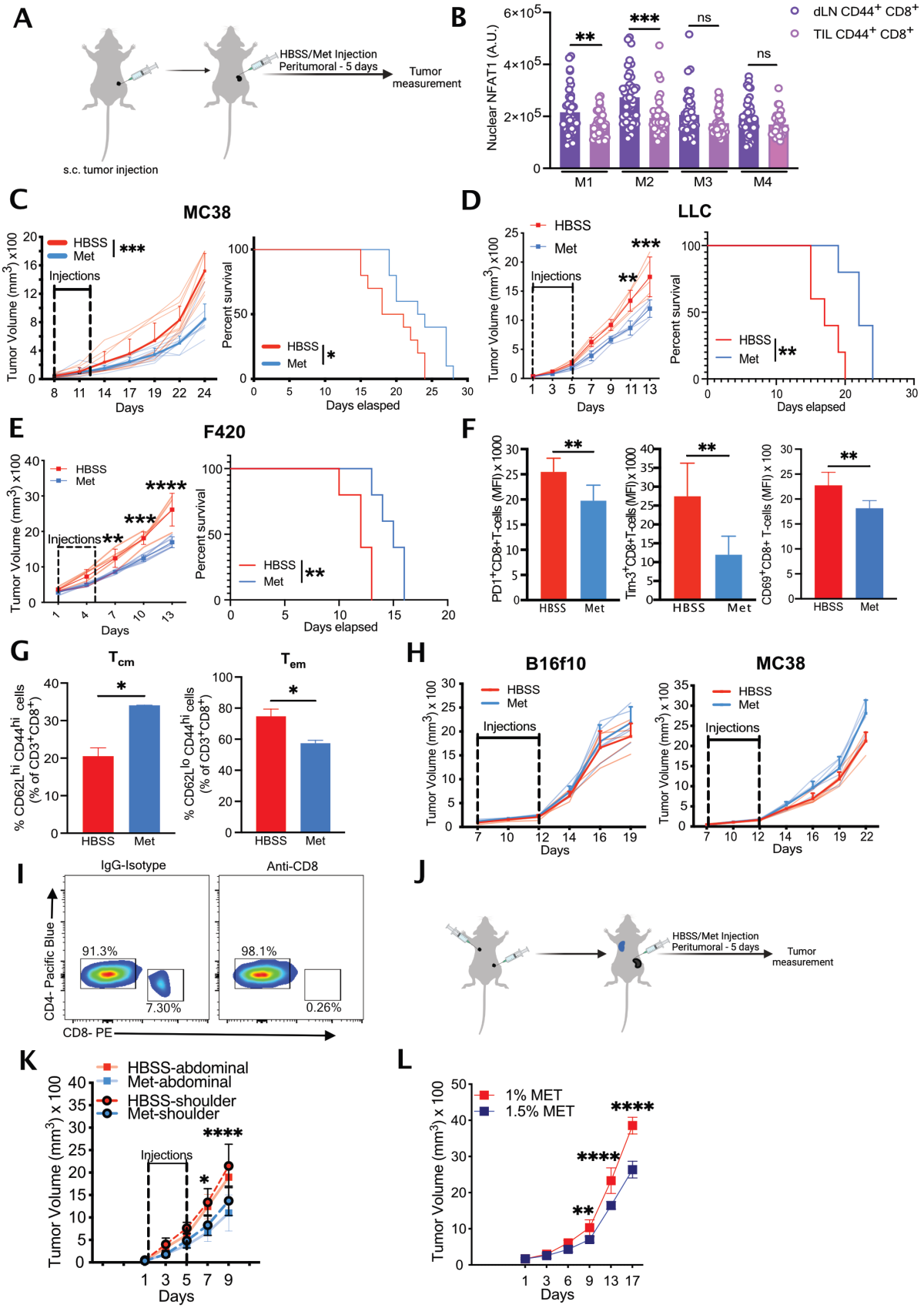

997

998 **Supplementary Fig. 10: Acute Met supplementation promotes anti-tumor T cell differentiation**
999 **and tumor control. (A)** Schematic of experimental design of acute HBSS/Met treatment in sub-
1000 cutaneous tumors. **(B)** Nuclear NFAT1 quantification of $CD44^+$ $CD8^+$ T cells isolated from B16
1001 subcutaneous tumors and dLN, 5 days post daily peri-tumoral supplementation of 50 μl 61μM
1002 Met (n=4 mice, each circle represents one cell, n=40 cells). **(C-E)** Tumor growth (left) and survival
1003 (right) of WT mice with sub-cutaneous MC38 colorectal tumors (c, n=10), Lewis-lung carcinoma
1004 (LLC) tumors (d, (representative of two experiments, n=5) and F420 osteosarcoma tumors (e,
1005 n=5), treated with either HBSS or 50 μl 61μM Met peri-tumorally daily for 5 days (n=10). **(F, G)**
1006 Expression of PD1, Tim-3, $CD69^+$ (f), Tcm ($CD62L^{hi}Cd44^{hi}$) and Tem ($CD62L^{lo}CD44^{hi}$) (g) on $CD8^+$ TIL
1007 isolated from B16 tumor bearing mice 2 days after 5 daily peri-tumoral injection with HBSS or
1008 Met (n=4). **(H)** Tumor growth of B16f10 and MC38 tumors in NSG mice treated peri-tumorally
1009 with 50 μl HBSS or 50 μl 61μM Met daily for 5 days (n=5). **(I)** Representative flow cytometry plot
1010 of blood showing $CD8^+$ T cell depletion in anti-CD8 antibody treated mice compared to IgG-
1011 Isotype treated mice (n=4). **(J)** Schematic of experimental design of contralateral tumor
1012 experiment. **(K)** Growth of B16f10 tumors implanted on left shoulder (dashed lines) and right
1013 flank (solid lines) following peri-tumoral injection of flank tumor with 50 μl HBSS or 61μM Met
1014 daily for 5 days (n=5, representative of two experiments). **(L)** B16 tumor growth in WT mice fed
1015 with either 1 % Met chow or 1.5 % Met chow, 7 days post tumor implantation (n=5). Data are
1016 mean±s.e.m. Two-way ANOVA (C-F, J and K), Mantel-Cox log rank test (C, D and E), unpaired two-
1017 tailed Student's t-test (B, G). *P < 0.05, **P < 0.01, ***P < 0.001, ****P < 0.0001.
1018
1019
1020
1021
1022

Supplementary Fig. 11

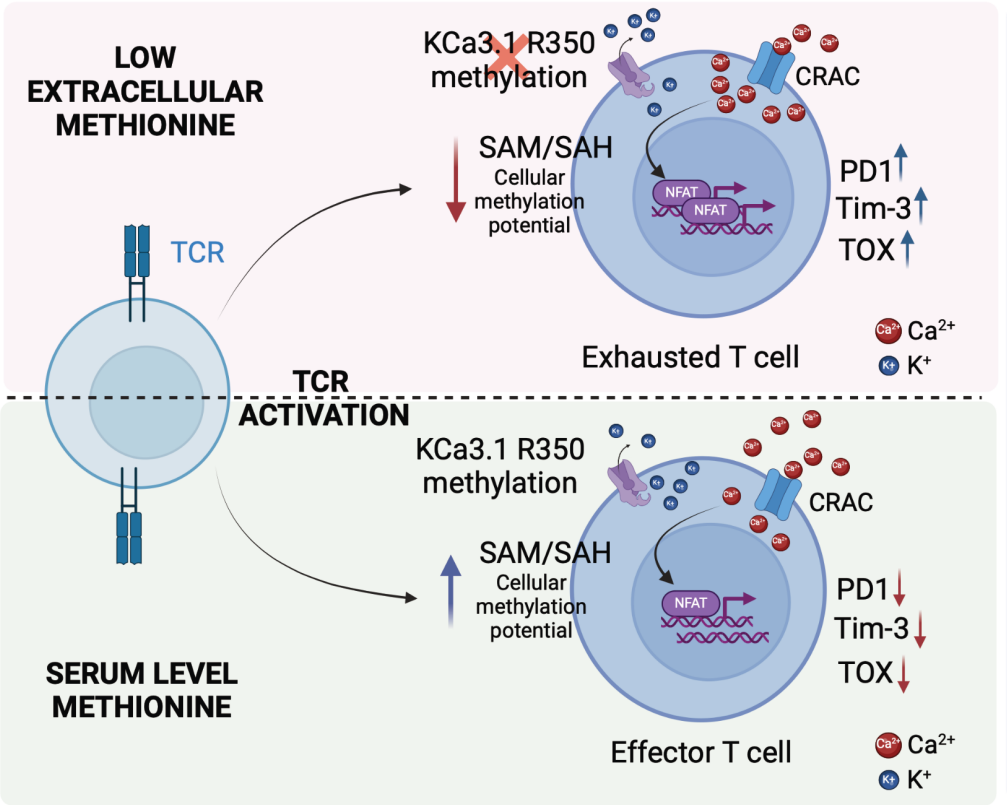

Supplementary Fig. 11: Methionine metabolism regulates TCR-mediated Ca^{2+} flux and T cell fate. Diagram illustrating the impact of methionine metabolism on TCR-dependent methylation of KCa3.1, leading to regulation of Ca2+ flux and subsequent activation of NFAT1. When extracellular Met levels are low, the potential for methylation decreases, which in turn reduces KCa3.1 methylation. This results in excessive channel activation and increased Ca2+ flux, ultimately triggering NFAT1 activation. NFAT1 then moves to the nucleus and activates gene signatures associated with activation and exhaustion, contributing to hyperactivation and exhaustion.

Materials and Methods:

Reagents

1035 RPMI 1640 (cat. 11875093, Gibco) and methionine-free RPMI 1640 (cat. A1451701; Gibco)
1036 supplemented with 10% dialyzed FCS (Atlanta Biologicals), sodium pyruvate (cat. 11360070,
1037 Gibco), NEAA (11140050, Gibco), glutamine (cat. 25030081, Thermo-Fisher), and penicillin-
1038 streptomycin cocktail (cat. 15070063, Thermo-Fisher) and stored at 4°C. Methionine (cat. M5308,
1039 Sigma-Aldrich) was reconstituted in PBS (0.1 M) and stored at 4°C. SIINFEKL peptide (cat. 60193,
1040 AnaSpec) peptide was reconstituted in PBS at 0.5 mg/ml and stored at -20°C. TRAM-34 (cat. HY-
1041 13519, MedChem Express) was reconstituted at 1 M with DMSO. Cyclosporin A (CsA) (cat. 30024,
1042 Sigma-Aldrich) was reconstituted to a concentration of 50 mg/ml in DMSO. YM-58483 (cat. 3939,
1043 Tocris) was reconstituted at 20 mM stock in DMSO. All reconstituted reagents were stored at -
1044 20°C and aliquoted to avoid repeated thawing.

1045 **Mice**

1046 All mouse studies were conducted in accordance with protocols approved by the St. Jude
1047 Children's Research Hospital Committee on Care and Use of Animals, and in compliance with all
1048 relevant ethical guidelines. All mice were kept under a 12h-12h light-dark cycle in a specific-
1049 pathogen-free (SPF) facility at the institute's Animal Resource Center. Age-and sex-matched
1050 mice were randomly assigned to the experimental and control groups. Cas9-OT/P14^{+}-I (Cas9
1051 Knock-in with OVA-specific transgenic TCR (OT-I) or LCMV-GP33 specific TCR(p14)), C57BL/6J
1052 (WT), OT-I, and Rag1$^{-/-}$ mice were bred in-house. The investigators were not blinded to the
1053 experiments and outcome assessments.

1054 **Cell lines**

1055 B16F10, B16F10-Ova (B16-Ova) melanoma cells were provided by Dr. Hongbo Chi. MC38 and
1056 MC38-Ova colon carcinoma cell lines were provided by Dr. Dario Vignali. The F420 sarcoma cell
1057 line was provided by Dr. Jason T Yustein. HEK293T and Lewis lung carcinoma (LLC) cells were
1058 purchased from the ATCC. Plat-e cells used for retroviral packaging were purchased from Cell
1059 Biolabs (cat. RV-101). All the cell lines used were tested and confirmed to be mycoplasma-
1060 negative but not independently authenticated.

1061 **Murine and Human CD8^{+} T cell isolation and stimulation**

1062 Murine $CD8^+$ T cells were isolated from the spleen and lymph nodes (LN) by physical disruption
1063 through a 70μ strainer before treatment with erythrocyte-lysis buffer. Cells were subjected to
1064 $CD8^+$ T cell enrichment using the EasySep mouse $CD8^+$ T cell isolation kit (cat. 19853, StemCell),
1065 according to the manufacturer's protocol. Isolated T cells were then either activated with
1066 SIINFEKL peptide or mouse CD3/28 Dynabeads (cat. 11456D, Thermo-Fisher) in RPMI medium, as
1067 described above. Human $CD8^+$ T cells were isolated from apheresis rings from the St Jude Blood
1068 Donor Center. Blood obtained from an apheresis ring was mixed at a 1:1 ratio with PBS containing
1069 2% FBS and carefully layered onto Lymphoprep (cat. 07801, StemCell) solution. The samples were
1070 then centrifuged at 800g for 30 min at room temperature without braking. The peripheral blood
1071 mononuclear cell (PBMC) layer was aspirated and washed twice in PBS with 2% FBS before
1072 enrichment of $CD8^+$ T cells using the Human $CD8^+$ T Cell Isolation Kit (cat. 17953, StemCell),
1073 according to the manufacturer's protocol. $CD8^+$ T cells were activated using human CD3/28
1074 Dynabeads (cat. 11131D, Thermo Fisher Scientific) in RPMI medium. Apheresis rings were
1075 collected with written consent from the donors for research upon review and approval by the
1076 Institutional Review Board at St Jude Children's Research Hospital.

1077 **Ca^{2+} Flux measurement**

1078 Isolated T cells were labelled with 3 µM Fluo-8 AM (AAT Bioquest, cat. 21080) or 5 µM ICR-1AM
1079 (Ion Biosciences) with 0.04% pluronic F-127 (Thermo-Fisher, cat. P6867) for 2 hrs in HHBS at 37 °C
1080 and washed twice with Ca^{2+}-free Krebs-Ringer's solution (Thermo Fisher Scientific, cat. no.
1081 J67839-AP). The cells were then resuspended in Ca^{2+}-free Krebs-Ringer's solution and incubated
1082 with anti-CD3ε (4 µg/ml; 2C11, cat. BE0001, Bio-X-Cell) and anti-CD28 (4 µg/ml; 37.51, cat.
1083 BE0015, Bio-X-Cell) on ice for 10 min. 0.1 mM Met or 0.03 mM Met was added to the samples
1084 and the baseline was recorded before the addition of hamster-IgG for crosslinking. Ca^{2+} influx was
1085 measured after the addition of 2mM Ca^{2+}, 1uM ionomycin was added as a positive control for
1086 Ca^{2+} flux. All measurements were recorded on either Cytek Aurora (SpectroFlo) or BD-Fortessa
1087 flow cytometer.

1088 **Quantitative PCR**

1089 Isolated T cells were activated with 2.5ng/ml SIINFEKL in 0.1 mM Met or 0.03 mM Met for 30 min
1090 after which Met in 0.03 mM was restored to 0.1 mM. T cells were then further cultured for 24
1091 hrs. Cells were washed twice with PBS and RNA was isolated using Direct-zol RNA miniprep Kit
1092 (Zymo research, cat. no. R2050). RNA was quantified and processed for cDNA synthesis using
1093 Reverse Transcriptase (Thermo Fisher Scientific, cat. no. 28025-013). cDNA was then used to
1094 perform quantitative PCR with the specific primers (Table S2) using SYBR green PCR master mix
1095 (Thermo Fisher Scientific, cat. no. 4309155). PCR reaction was run and quantified by QuantStudio
1096 7 flex.

1097 **Cloning and virus production**

1098 *Kcnn4* gRNA's were designed using the Broad Institute platform
1099 (https://portals.broadinstitute.org/gpp/public/analysis-tools/sgrna-design) and cloned into the
1100 ametrine-expressing retroviral vector LMPd-gRNA-mPGK-Ametrine
1101 (sgRNA1:CACCGGGCAGGCTGTCAATGCCACG, AAACCGTGGCATTGACAGCCTGCCC;
1102 sgRNA2:CACCGTGTGGGGCAAGATTGTCTGC, AAACGCAGACAATCTTGCCCCACAC). KCa3.1^{WT} and
1103 KCa3.1^{R350A} cDNA were synthesized by Genscript; the latter contained an alanine substitution at
1104 R350. Both KCa3.1^{WT} and KCa3.1^{R350A} had substitutions at the PAM recognition sites of the gRNAs
1105 (Table S3). Each cDNA was subcloned into the pMIGII. Plat-e cells were co-transfected with the
1106 cloned vectors and pCL-eco (cat. 12371, Addgene) in Opti-MEM (cat. 31985070, Thermo-Fisher)
1107 with Trans-IT-293 transfection reagent (cat. MIR 2705, Mirus Bio) and cultured at 37°C for 12-15
1108 hrs prior to changing the medium and culturing for an additional 24 hrs at 37°C, followed by 24
1109 hrs at 32°C, 5% CO_2. The viral supernatant was harvested and spun at 1800rpm at RT to remove
1110 the cell debris. Viral supernatant was either used immediately or stored at -80°C till further use.

1111

1112 **Viral transduction**

1113 Naive Cas9-OT-I CD8$^+$ cells were isolated from the spleen and peripheral LNs of Cas9-OT-I mice
1114 using a Magnisort naïve CD8$^+$ T cell isolation kit according to the manufacturer's instructions (cat.
1115 8804-6825-74, Thermo-Fisher). Purified CD8$^+$ T cells were activated *in vitro* for 20 h with plate-

1116 bound anti-CD3ε (5 μg/ml; 2C11, cat. BE0001, Bio-X-Cell) and anti-CD28 (5 μg/ml; 37.51, cat.
1117 BE0015, Bio-X-Cell) antibodies. Viral transduction was performed by spinfection at 900 *g* at 25 °C
1118 for 3 h with 10 μg/ml polybrene (Sigma-Aldrich), followed by resting for 3 h at 37 °C in 5% CO_2.
1119 Cells were washed and cultured in medium supplemented with mouse rIL-2 (20 U/ml; cat. 212-
1120 12, Peprotech) for 4 days. GFP-Ametrine double-positive cells were sorted using the Reflection
1121 cell sorter (iCyt) or the MoFlo XDP cell sorter and rested for 24 hrs in medium containing rIL-2
1122 (10U/ml, cat. 212-12 Peprotech) before activation or adoptive transfer into the animals.

1123 **Flow cytometry**

1124 Antibodies from BioLegend included Pacific Blue anti-mouse Ly108 (330-AJ, 134608), BV510 anti-
1125 mouse KLRG1 (2F1, 138421), BV570 anti-mouse CD62L (MEL-14, 104433), BV711 anti-mouse Tim-
1126 3 (RMT3-23, 119727), BV785 anti-mouse CD127 (A7R34, 135037), PE-Cy5 anti-mouse Granzyme-
1127 B (QA16A02, 372226), PE-Fire 700, anti-mouse CD4 (GK1.5, 100484), APC/Cy7 anti-mouse TNFα
1128 (MP6-XT22, 506344), PE-Cy7 anti-mouse KLRG1 (2F1/KLRG1, 138416), PerCP-Cy 5.5 anti-mouse
1129 CD62L (MEL-14, 104432), BV605 anti-mouse CD127 (A7R34, 135025), Pacific blue anti-mouse
1130 CD69 (H1.2F3, 104524), Pacific blue anti-mouse CD45.1 (110722), APC anti-mouse PD1 (RL388,
1131 109111), BV711 anti-mouse PD1 (29F.1A12, 135231), PE anti-mouse IFNγ (XMG1.2, 505808), FITC
1132 anti-mouse TNFα (MP6-XT22, 506304), Pacific Blue anti-human CD45 (HI30, 982306), APC/Cy7
1133 anti-human CD8 (RPA-T8, 344713). BUV563 anti-mouse LAG3 (C9B7W, 741350), BUV615 anti-
1134 mouse CD69 (H1.2F3, 751593), BUV805 anti-mouse CXCR3 (173, 748700), BV421 anti-mouse
1135 EOMES (X4-83, 567166), BV480 anti-mouse CD45.1 (A20, 746666), Alexa-Fluor 488 anti-mouse
1136 TCF1 (S33-966, 567018), Alexa-Fluor 647 TOX (NAN448B, 568356), BUV 496 anti-mouse Ly-108
1137 (13G3, 750046), APC/Cy7 anti-mouse CD44 (IM7, 560568) and BUV805 anti-mouse CD8α (53-6.7,
1138 612898) were acquired from BD Biosciences. BUV395 anti-mouse CD44 (IM7, 363-0441-82),
1139 PerCP-Cy 5.5 anti-mouse IL-2 (JES6-5H4, 45-7021-82), PerCP-eF710 anti-mouse CD27 (O323, 46-
1140 0279-42), and PE-Cy7 anti-mouse Tim-3 (RMT3-23, 12-5870-82, eBioscience) were obtained from
1141 Thermo Fisher. APC anti-human/mouse Tox (REA473, 130-118-335) was obtained from Miltenyi
1142 Biotech. For surface markers, the cells were stained for 30 min on ice in PBS containing 2% FCS
1143 and 0.1% sodium azide (cat. S2002, Sigma-Aldrich). To examine intracellular cytokine production,

1144 the isolated cells were stimulated with a cell activation cocktail (cat. 5476, TOCRIS) in the
1145 presence of monensin (cat. 554724, BD Biosciences) for 4 hr, and stained for intracellular
1146 cytokines and transcription factors using a fixation/permeabilization kit (cat. 00-5523-00,
1147 Ebiosciences). Fixable viability dye (Thermo Fisher) was used to exclude dead cells. Samples were
1148 acquired on a Cytek Aurora (SpectroFlo) or BD LSRII (FACSDiva) flow cytometer and analysed
1149 using FlowJo software.

1150 ***In vivo* tumor analysis**

1151 For all tumor experiments, $0.5x10^6$ tumor cells were injected subcutaneously into the right flank
1152 of naive mice (aged 6–10 weeks). Met was diluted in HBSS to a concentration of 61 µM per 50µl.
1153 Mice were injected peri-tumorally for 5 days with either 50 µl Met or HBSS. Tumours were
1154 measured with calipers every 2 days and tumor volumes were calculated using the formula:
1155 $(\text{width}^2 \times \text{length})/2$. For adoptive transfer experiments, T cells (1×10^6) were transferred i.v. 7 -9
1156 days after tumor injection. For contralateral tumor model, 0.5×10^6 B16 tumor cells were
1157 injected subcutaneously into the right flank and left shoulder of the same mouse. Met or HBSS
1158 was injected peri-tumorally to the right flank tumor (abdominal). For check-point blockade
1159 experiment, 0.5×10^6 MC38 tumor cells were injected subcutaneously into the right flank of WT
1160 mice. The mice were given either anti-PD1 antibody (RMP1-14, Bio X Cell) or rat IgG2a (2A3, Bio
1161 X Cell), intraperitoneally twice at a dose of 150 mg/kg in 100 µl PBS at day 9 and 12. Met or HBSS
1162 was given peri-tumorally for 5 days from day 9 to 13. For the CAR-T tumor model, 0.5×10^6 F420
1163 tumor cells (derived from singly floxed *p53+/F-Col2.3* transgenic mice(*1*)); were injected
1164 subcutaneously into the right flank of $Rag1^{-/-}$ mice. 5×10^6 B7-H3 CAR-T cells (see below) were
1165 transferred i.v. 8-10 days post implantation. Tumour size was measured every 2-4 days.

1166 **Generation of mouse CAR-T cells**

1167 Generation of mouse B7-H3-CAR constructs and CAR-T generation have been previously
1168 described(*2*). Briefly, HEK293T cells were transiently transfected with the CAR-encoding plasmid,
1169 the Peg-Pam plasmid encoding MoMLV gag-pol, and a plasmid encoding the VSVG envelope. Viral
1170 supernatants were collected at 48 h and filtered with a 0.45m filter. The virus was then used to

1171 transduce the GPE86 producer cell line. B7-H3-CAR-expressing GPE86 cells were stained with
1172 Alexa Fluor-647 anti-human IgG, F(ab')2 fragment antibody (cat. 109-606-006, Jackson
1173 ImmunoResearch) and sorted using the BD FACSAria III system.

1174 Naive $CD8^+$T cells from 6–8 weeks old $CD45.1^+$ mice were activated with plate-bound anti-CD3ε
1175 (1 µg/ml, 145-2C11, cat. BE0001, BioXcell), anti-CD28 (2 µg/ml, 37.51, cat. BE0015, BioXcell) and
1176 50 U ml^{-1} rhIL-2 (cat. 200-02, Peprotech). On day 2 post activation, activated $CD8^+$ T cells were
1177 transduced with retrovirus expressing B7-H3-CAR on retronectin-coated (cat. T100B, Takara)
1178 non-tissue-culture-treated plate in complete RPMI medium supplemented with 50 U/ml rhIL-2.
1179 At 48 h after transduction, CAR-T cells were collected and expanded in the presence of
1180 50 U/ml rhIL-2 for another 3 days before adoptive transfer into tumor-bearing mice.

1181 **Tumour-infiltrating lymphocyte isolation**

1182 B16 tumors were harvested at the indicated time points and digested using a digestion cocktail
1183 (0.1% Collagenase IV and 0.01% DNaseI) for 5 min at 37 °C. Digested tumors were passed through
1184 a 70m strainer and resuspended in PBS plus 2% dialyzed FCS and processed for analysis and/or
1185 sorting by flow cytometry, as described above.

1186 Patient samples were collected following surgery and were immediately processed. Tumour
1187 samples were dissected into small pieces and digested at 37°C with digestion cocktail for 40 min.
1188 Digested tumor samples were physically disrupted and passed through 70µ filter. Samples were
1189 washed with PBS-2% dialyzed FCS twice and stained for CD45, CD3ε and CD8 and sorted for $CD8^+$
1190 T cells by flow cytometry. Purified T cells were washed once with 1% saline and flash frozen in
1191 liquid nitrogen. Samples were collected upon informed consent and procedures approved by the
1192 IRB of St. Jude Children's Research Hospital.

1193 **Immunofluorescence staining and imaging.**

1194 $CD8^+$ T cells were immobilized in 8-well poly L-lysine-coated IBIDI chambers and stimulated by
1195 the addition of CD3/28 Dynabeads (cat. 11452D, Thermo Fisher) for 30 min, followed by 10 min
1196 of fixation with 4% paraformaldehyde (PFA) (cat. 15710, Electron Microscopy Science) at 37°C.

1197 The cells were washed once with TBS (50 mM Tris, 100 mM NaCl, pH 8.0) and permeabilized with
1198 permeabilization buffer (50mM Tris, 100 mM NaCl, pH 8.0, 0.3% (v/v) Triton X-100) for 20 min at
1199 room temperature. Cells were washed again with TBS before blocking with TBS containing 2%
1200 BSA (Cat. 001-000-182, Jackson ImmunoResearch) for 60 min at room temperature. The cells
1201 were stained overnight at 4 °C with the following primary antibodies: anti-NFAT1 (1:200, cat.
1202 4389, Cell Signaling Technology), anti-NFAT2 (1:200, cat. D15F1, Cell Signaling Technology) and
1203 anti-mono and dimethyl arginine (1:500, cat. ab412, Abcam). The samples were washed twice
1204 with TBS and incubated for 1 h at room temperature with the following antibodies: anti-rabbit
1205 Alexa Fluor plus 595 (1:1,000, cat. A-11012, Thermo Fisher), anti-mouse CD8-APC (1:500; cat.
1206 100712, BioLegend), Alexa Fluor 488 Phalloidin (1:1000, cat. A12379, Thermo Fisher) and Hoechst
1207 33258 (1:1000, cat. H3569, Thermo-Fisher). Samples were then imaged by Marianas spinning-
1208 disc confocal microscopy (Intelligent Imaging Innovations), using the Prime95B sCMOS camera,
1209 and the 405, 488, 561 and 640 nm laser lines. Sum fluorescence intensities were analyzed using
1210 Slide Book 6 (Intelligent Imaging Innovations).

1211 **Immunoblotting**

1212 T cells were washed once with ice-cold PBS and immediately lysed with 4x laemmli buffer (Bio-
1213 Rad, cat. 1610747). Cell lysates were separated by SDS-PAGE and blotted with anti-Kcnn4
1214 antibody (cat. PA5-33875, Thermo Fisher) and HRP-conjugated anti-Actin (cat. sc4777-HRP, Santa
1215 Cruz Biotechnology). Images were developed using Clarity Western ECL substrate (cat. 1705061,
1216 Bio-Rad) and acquired on Bio-Rad Chemi-Doc.
1217

1218 **Amino acid measurement**

1219 Subcutaneous tumors were isolated and processed as described above. Sorted T cells were
1220 washed once with ice-cold saline, flash-frozen with liquid nitrogen, and stored at –80ºC before
1221 analysis. Cell pellets were extracted using 750 µl of methanol/acetonitrile/water (5:3:2, v/v/v)
1222 and the supernatant was dried by lyophilization. Aliquots of 20-50 µl from plasma and TIF were
1223 extracted with at least a 15-fold excess volume of the methanol/acetonitrile/water solution, and

1224 the supernatant was then collected and dried by lyophilization. Dried extracts containing the
1225 hydrophilic metabolites were dissolved in 30 µl of water/acetonitrile (8:2, v/v), and 10 µl was
1226 used to derivatize amino acids as described (*3*) with some modifications. The samples were
1227 placed in glass autosampler vials, and 35 µl of sodium borate buffer (100 mM, pH 9.0) was added
1228 and mixed by pipetting. 10 µl of the 6-aminoquinolyl-N-hydroxysuccinimidyl carbamate (AQC, 10
1229 mM in acetonitrile)-derivatizing reagent (Cayman Chemical) was added, the vial was sealed,
1230 mixed by vortexing, and then incubated at 55°C for 15 min. The vial was cooled to room
1231 temperature and then 1 µL was analyzed by liquid chromatography with tandem mass
1232 spectrometry (LC-MS/MS). An ACQUITY Premier UPLC System (Waters Corp) was used for the LC
1233 separations, using a non-linear gradient condition as follows: 0-0.4 min 3% B; 0.4-8 min 3 to 96%
1234 B (using Curve #8 of the inlet condition in MassLynx™); 8-12 min 96% B; 12-12.5 min 96 to 3% B;
1235 12.5-14 min 3% B. Mobile phase A was water supplemented with 0.15% acetic acid, and mobile
1236 phase B was acetonitrile with 0.15% acetic acid. The column used was an Accucore C30 (50 × 2.1
1237 mm, 2.6 µm) (Thermo Fisher Scientific) operated at 50°C. The flow rate was 300 µl/min and the
1238 injection volume used was 1 µl. All LC/MS solvents and reagents were the highest purity available
1239 (water, acetonitrile, acetic acid, boric acid, sodium hydroxide) and were purchased from Thermo
1240 Fisher Scientific. A Xevo TQ-XS Triple Quadrupole Mass Spectrometry (TQ-XS) (Waters Corp)
1241 equipped with a multi-mode ESI/APCI/ESCi ion source was employed as detector. The TQ-XS was
1242 operated in positive ion mode using a multiple reaction monitoring mass spec method (MRM).
1243 The MRM conditions were set to a minimum of 15 points per peak with an automatic dwell time.
1244 The operating conditions of the source were: Capillary Voltage 3.8 kV, Cone Voltage 40 V,
1245 Desolvation Temp 550°C, Desolvation Gas Flow 1000 L/h, Cone Gas Flow 150 L/h, Nebuliser 7.0
1246 Bar, Source Temp 150°C. Authentic amino acid standards were purchased from Sigma-Aldrich
1247 and used to establish MRM conditions and calibration curves. The monitored parent/daughter
1248 ions, fragmentation collision energy (CE), and retention time window for each amino acid are
1249 listed in Supplementary Table 4. The acquired MRM data was processed using the software
1250 application Skyline 21.2 (MacCoss Lab Software).
1251
1252 ***In-silico* model building of KCa3.1(SK4)-Calmodulin complex and simulation.**

1253

1254 To study the impact of SK4s arginine dimethylation on the binding of calmodulin, we simulated
1255 the SK4 channel:Calmodulin complex in a membrane layer via all-atom molecular dynamics (MD),
1256 which is considered a computational microscope(*4*). The Cryo-EM structure of the human SK4
1257 channel:Calmodulin complex state (PDB:6CNN(*5*)) was used as the starting structure. Thisa
1258 tetramer compleconsistsng of four SK4 monomers, four calmodulins (CAMs), three calcium ions
1259 bound to each calmodulin (CAM) (total 1,2) and four K^+ ions bound to the channel selectivity
1260 filter.

1261 Initially, protein was prepared was using the molecular operating environment (MOE) software.
1262 The missing residues in the cryo-EM structure were modeled based on the human AlphaFold
1263 structure (AF-015554-F1). Protonate3D module in MOE was used to assign appropriate
1264 protonation states at pH 7.4 and then energy minimized. Further, simulation system was
1265 prepared using CHARMM-GUI web server(*6-8*). Protein was placed in the POPE membrane bilayer
1266 and protein orientation was obtained using the PPM web server(*9*). The protein-membrane
1267 bilayer complex was immersed in the TIP3P(*10*) water box of size ≈150 X 150 X 230 $Å^3$ with an
1268 edge distance of 40 Å on all sides. KCl salt was added to balance the charges and maintain a
1269 physiological salt concentration of 0.15M. Overall, each wildtype simulation system contains four
1270 SK4 monomers, four CAMs, 12 Ca^{2+} ions, ≈355 K^+ ions, ≈367 Cl^- ions, ≈618 POPE lipids, and
1271 ≈128,144 TIP3P waters. The total numbers of atoms in this system are ≈498,944. Two more
1272 systems were generated via a protocol similar to that explained above, except that in one system,
1273 R352 of the SK4 monomer was symmetrically dimethylated and in the second system, R352 was
1274 asymmetrically dimethylated. Dimethylation was introduced using the CHARMM-GUI web
1275 server. Note that arginine's at position 352 in all four SK4 monomers were dimethylated in both
1276 systems.

1277 Further, all three systems were simulated using AMBER20/22 MD software(*11*). The MD
1278 simulation was performed in three steps. In step-1, energy minimization was carried out to
1279 remove potential steric clashes in two stages. In stage 1, each system was energy-minimized for
1280 5000 steps, while positional restraints were applied to the protein and membrane: the first 2500
1281 steps with the steepest-descent algorithm and the remaining 2500 steps using the conjugate
1282 gradient algorithm(*12*). In stage 2, the second round of minimization was carried out with all

1283 restraints removed in 50,000 steps. The steepest-descent algorithm(*13*) was used for the first
1284 25,000 steps, while the conjugate gradient algorithm was used for the remaining 25,000 steps.
1285 In step-2, equilibration was carried in six stages: (1) equilibrated for 125 ps with a time step of
1286 1fs while applying positional restraints on protein (K=10 kcal/mol.Å^2) and membrane (K=2.5
1287 kcal/mol.Å^2), (2) equilibrated for 125 ps with a time step of 1fs w while applying positional
1288 restraints on the protein (K=5.0 kcal/mol.Å^2) and membrane (K=2.5 kcal/mol.Å^2), (3) equilibrated
1289 for 125 ps with a time step of 1fs while applying positional restraints on the protein (K=2.5
1290 kcal/mol.Å^2) and membrane (K=1.0 kcal/mol.Å^2), (4) equilibrated for 500 ps with a time step of 2
1291 fs while applying positional restraints on the protein (K=1.0 kcal/mol.Å^2) and membrane (K=0.5
1292 kcal/mol.Å^2), (5) equilibrated for 500 ps with a time step of 2 fs while applying positional
1293 restraints on the protein (K=0.5 kcal/mol.Å^2) and membrane (K=0.1 kcal/mol.Å^2) and (6)
1294 equilibrated for 500 ps with a time step of 2 fs while applying weak positional restraints on the
1295 protein (K=0.5 kcal/mol.Å^2) and restraints on the rest of the system were completely removed.
1296 The first two equilibration simulations were performed under NVT conditions, whereas the last
1297 four equilibration simulations were performed under NPT conditions. In step-3, production
1298 simulations were carried out under periodic boundary conditions using the NPT ensemble, during
1299 which the temperature (310 K) and pressure (1 atm) were kept constant. Three replicates of each
1300 system were simulated, and each replicate was simulated for ≈1 µs. Langevin integrator and
1301 Monte Carlo barostat were used(*14, 15*) to conduct NPT simulations, whereas the SHAKE
1302 algorithm was used to restrain bonds with hydrogens(*16*). Particle-mesh Ewald (PME) method
1303 was used to treat long-ranged electrostatic interactions(*17*) and the nonbonded cutoff was 12Å
1304 (force switching = 10Å). CHARM36 all-atom additive force field(*18, 19*) was used to treat the
1305 entire system. Overall, nine MD simulations were conducted across three systems, with each
1306 system comprising three replicates that each ran for approximately 1µs. Consequently, the total
1307 MD simulation data accumulated for analysis amounts to approx. 9 µs, derived from the sum of
1308 simulation times for all systems and replicates (3 systems X 3 replicates X ≈1µs/per replicate =
1309 ≈9µs). Two frames per nanosecond were used for the data analysis. Visual molecular dynamics
1310 (VMD)(*20*) was used for visualization and graphic generation, whereas Tcl was used for data
1311 analysis. Gnuplot was used to generate the time series plots.

1312

1313 **ATAC-seq**

1314 OT-I CD8$^+$ T cells were activated with 2.5ng/ml SIINFEKL in either 0.1 mM Met or 0.03 mM Met
1315 with restoration of Met to 0.1 mM in 0.03 mM condition post 30 min of activation and incubated
1316 for 24 hrs. KCa3.1^{WT} and KCa3.1^{R350A} cells were activated by 2.5ng/ml SIINFEKL for 24 hrs. Cells
1317 were processed for ATAC-Seq after 24 hrs of activation. Briefly, 50,000 cells were washed with 1
1318 ml cold PBS by centrifugation at 500 g for 5 min at 4°C. Cells were then resuspended in 50 ml cold
1319 cell lysis buffer (10 mM Tris pH 7.4, 10 mM NaCl, 3 mM $MgCl_2$, and 0.1% NP-40). Isolated nuclei
1320 were pelleted at 1,000 × g for 10 min at 4°C, resuspended in 50 µl transposition reaction mixture
1321 (25 µl TD buffer, 2.5 µl TDE1, 22.5 µl ddH_2O) (20034197, Illumina), and incubated at 42°C for 45
1322 min. DNA was purified using a MiniElute PCR purification kit (cat. 28004, Qiagen). Samples were
1323 then processed for library barcoding and amplification with Q5 High-Fidelity 2× Master Mix (cat.
1324 M0492S, NEB). Prepared libraries were sent for sequencing after quantification using Qubit and
1325 size distribution as determined using an Agilent 4200 TapeStation.

1326 **Analysis of ATAC-seq data**

1327 Paired-end sequencing reads were trimmed using Trim Galore (version 0.5.0)
1328 (https://github.com/FelixKrueger/TrimGalore) with default parameters. Reads were aligned to the
1329 reference mouse mm10 assembly using Bowtie 2 (version 2.3.5.1)(*21*) with settings --end-to-end -
1330 -very-sensitive -X 2000. The resulting alignments, recorded in a BAM file, were sorted, indexed,
1331 and marked for duplicates with Picard MarkDuplicates function (version 2.19.0). Afterward, the
1332 BAM file was filtered with SAMtools (version 1.9)(*22*), BamTools (version 2.5.1)(*23*) and scripts
1333 of nf-core/chipseq(*24*) to discard reads, mates that were unmapped, PCR/optical duplicates, not
1334 primary alignments, mapped to multiple locations, or mapped to ENCODE blacklisted
1335 regions(*25*); only reads mapped in proper pair were kept (-F 1804 -f 2 -q 30). The alignments were
1336 shifted by deepTools alignmentSieve(*26*) with --ATACshift and default parameters. Nucleosome-
1337 free reads (fragment length < 109 bp) were separated from the BAM files with SAMtools (version
1338 1.9). MACS (version 2.1.2)(*27*) was used to call peaks from the BAM files with narrowPeak
1339 setting, --extsize 200, and recommended mappable genome size (default value for other

1340 parameters). Chromatin accessibility signal was normalized by scaling to 1 million mapped reads
1341 using BEDTools (version 2.27.1)(*28*) and bedGraphToBigWig (version 377)(*29*) and visualized
1342 as heatmaps using deepTools plotHeatmap (version 3.2.1)(*26*).

1343 Differentially accessibility analysis was performed using DiffBind(*30*) (v.3.4.7) (summit = 50,
1344 normalized by trimmed mean of M values(*31*) (TMM) approach, library size estimated by reads
1345 mapped to "background" regions, the genomic regions (binned into 15000 bp) overlapped with
1346 peaks). Peaks were annotated to the nearest genes with annotatePeak function in R package
1347 ChIPseeker(*32*) (v.1.30.3) at the gene level using the default parameters. Genes were ranked by
1348 fold change (log2 transformed) of associated peaks located within +/- 1.5 kb of transcription start
1349 sites (if a gene was associated with multiple peaks, the mean was used). Gene Set Enrichment
1350 Analysis(*33*) (GSEA) was then performed against MSigDB collections with R package
1351 clusterProfiler(*34*) (v.4.2.2). The common differentially accessible regions (DAR) between ATAC-
1352 Seq of KCa3.1WT and KCa3.1R350A and T cells activated in 0.1 mM or 0.03 mM Met were
1353 obtained by the overlapping of the DARs (at least 1 bp). Enrichment analysis was performed using
1354 the over-representation approach against MSigDB using the R package clusterProfiler.

1355 **CUT&RUN**

1356 CUT&RUN experiments were performed as previously described(*35*) with slight modifications.
1357 Purified OT-I $CD8^+$ T cells were activated with 2.5ng/ml SIINFEKL in 0.1 mM and 0.03 mM Met for
1358 30 min. Met was restored to 0.1 mM post 30 min and cultured for 24 hrs. Cells were washed with
1359 cold PBS and dead cells were removed using Easysep dead cell removal kit (cat. 17899, StemCell).
1360 Cells (2×10^5) were washed twice with wash buffer (20 mM HEPES (H3375, Sigma-Aldrich],
1361 150 mM NaCl (cat. AM9760G, Invitrogen), 0.5 mM spermidine (cat. S0266, Sigma-Aldrich), and
1362 protease inhibitor cocktail (cat. 5056489001, Sigma-Aldrich)), resuspended and bound to
1363 concanavalin-A coated magnetic beads (cat. BP531, Bang Laboratories). The resuspension buffer
1364 was removed using a magnetic stand and beads were resuspended in 100 µl antibody buffer
1365 (20 mM HEPES, 150 mM NaCl, 0.5 mM spermidine, 0.01% digitonin (cat. 300410, Millipore),
1366 2 mM EDTA (cat. AM9260G, Invitrogen), and protease inhibitor cocktail). Primary antibodies
1367 (1:100) were added to the samples and incubated overnight at 4 °C. Next, samples were washed

1368 twice with cold Dig-wash buffer (20 mM HEPES, 150 mM NaCl, 0.5 mM spermidine, 0.01%
1369 digitonin, and protease inhibitor) and pAG-MNase (cat. 123461, Addgene) was added and rotated
1370 at 4 °C for 1 h. Samples were washed twice and resuspended in 50 µl Dig-wash buffer and
1371 $CaCl_2$ (2 µl of 100 mM, cat. 2115, Sigma-Aldrich) was added followed by brief vortexing and
1372 incubation on ice for 30 min. Next, 50 µl of 2× STOP buffer (340 mM NaCl, 20 mM EDTA, 4 mM
1373 EGTA (cat. E3889, Sigma-Aldrich) and 100 µg/ml RNase A (cat. EN0531, Thermo Fisher), and
1374 50 µg/ml GlycoBlue (cat. AM9515, Invitrogen)) was added and mixed by gentle vortexing and
1375 incubated for 30 min at 37 °C to release CUT&RUN fragments. Fragmented DNA was purified
1376 using the NEB Monarch PCR&DNA Cleanup Kit (cat. T1030S, New England Biolabs). DNA libraries
1377 were prepared using the NEBNext Ultra II DNA Library Prep Kit (cat. E7645S, New England Biolabs)
1378 and purified with AMPure SPRI beads (cat. B23318, Beckman-Coulter). Prepared libraries were
1379 quantified using Qubit and size distribution was determined with a Agilent 4200 TapeStation
1380 analysis before paired-end sequencing.

1381 **CUT&RUN data processing**

1382 Paired-end sequencing reads were trimmed using Trim Galore (v.0.5.0)
1383 (https://github.com/FelixKrueger/TrimGalore) with default parameters. The reads were then
1384 aligned to the reference mouse mm10 assembly using Bowtie 2 (v.2.3.5.1)(*21*) with settings --end-
1385 to-end --very-sensitive --no-mixed --no-discordant -q --phred33 -I 10 -X 700. The resulting
1386 alignments, recorded in the BAM file, were sorted, indexed, and marked for duplicates using the
1387 Picard MarkDuplicates function (v.2.19.0) (Picard toolkit. *Broad Institute GitHub Repository,*
1388 2019). Next, the BAM file was filtered with SAMtools (v.1.9)(*22*), BamTools (v.2.5.1)(*23*) and
1389 scripts of nf-core/chipseq(*24*) to discard reads, including mates that were unmapped, PCR/optical
1390 duplicates, non-primary alignments, reads that mapped to multiple locations or to ENCODE-
1391 blacklisted regions(*25*), or with more than 4 mismatches (-F 0x004 -F 0x008 -F 0x0100 -F 0x0400
1392 -f 0x001 -q 1). MACS (v.2.1.2)(*27*) was used to call peaks from the BAM file with IgG control
1393 and recommended mappable genome size (the default values were used for the other parameters).
1394 NarrowPeak mode was used for NFAT1, H3K27me3, and H3K4me3. Binding signal was
1395 normalized by scaling to 1 million mapped reads using BEDTools (version 2.27.1)(*28*) and

1396 bedGraphToBigWig (version 377)(*29*) and visualized as heatmaps using deepTools plotHeatmap
1397 (version 3.2.1)(*26*)

1398 In the CUT&RUN experiment with spike-in E. coli, two modifications were made: i) a hybrid
1399 reference of mouse mm10 and E. coli ASM584v2, and ii) signals were normalized by scaling to
1400 per million reads mapped to E. coli.

1401 Differential binding analysis was performed using DiffBind (v.3.4.7) (summit = 75 (for NFAT1) and
1402 100 (for H3K27me3 and K3K4me3 modifications), normalized by the trimmed mean of M values
1403 (TMM) approach library size estimated by reads mapped to "background" regions. Peaks were
1404 annotated to the nearest genes with the annotatePeak function in R package ChIPseeker
1405 (v.1.30.3) at the gene level using default parameters. Genes were ranked by fold-change (log2
1406 transformed; if a gene was associated with multiple peaks, the mean was used). GSEA was then
1407 performed against MSigDB collections with R package clusterProfiler (v.4.2.2).

1408 **RNA-seq**

1409 The isolated $CD8^+$ TIL were washed once with cold PBS and pelleted at 1500 rpm at 4°C. Total
1410 RNA was isolated using the Direct-zol RNA Microprep Kit (cat. R2061, Zymo Research) according
1411 to the manufacturer's instructions and quantified using an Agilent 4200 TapeStation. Libraries
1412 were prepared using the KAPA RNA HyperPrep Kit with RiboErase (HMR) (cat. 08098131702,
1413 Roche) and purified by AMPure SPRI beads (cat. B23318, Beckman-Coulter). Libraries were
1414 quantified and size distribution was determined using a Agilent 4200 TapeStation before paired-
1415 end sequencing was performed.

1416 **RNA-seq data processing**

1417 Paired-end sequencing reads were mapped by the pipeline of St. Jude Center for Applied
1418 Bioinformatics. The reads were trimmed using Trim Galore (version 0.5.0)
1419 (https://github.com/FelixKrueger/TrimGalore) with default parameters. Reads were aligned to
1420 the reference mouse mm10 assembly plus ERCC spike-in sequences using STAR (version
1421 2.7.5a)(*36*). The resulting alignments, recorded in BAM file, were sorted, indexed, and marked
1422 for duplicates with Picard MarkDuplicates function (version 2.19.0). Transcript quantification was

1423 calculated using RSEM(*37*). Differential gene expression analysis was carried out with DESeq2
1424 with Wald test (default parameters)(*38*). To examine if global changes in gene expression were
1425 present, the RUVg function in the RUVSeq package was used for normalization with ERCC spike-
1426 in followed by DESeq2 according to the RUVSeq manual(*39*). Gene set enrichment analysis (GSEA)
1427 was performed against the MSigDB database(*40*) with R package clusterProfiler (version
1428 4.2.2)(*34*) with the genes ranked by the Wald statistic from DESeq2 analysis.

1429

1430 **Quantitative Proteomics by tandem mass tag mass spectrometry (TMT-MS)**

1431 $CD8^+$ T cells were isolated from WT mice and activated with anti-CD3 antibody by crosslinking
1432 with IgG for 30 min. Activated and untreated cells were washed once with ice-cold PBS and flash-
1433 frozen in liquid nitrogen. Proteomic profiling of the whole proteome and methylome was carried
1434 out using a previously optimized protocol(*41*) with modifications. Briefly, the cells were lysed in
1435 8M Urea lysis buffer using pulse sonication, and approximately 100 µg of protein per sample was
1436 digested with Lys-C (Wako, 1:100 w/w) at 21 °C for 2 h, followed by dilution to reduce urea to
1437 2M, and further digestion with trypsin (Promega, 1:50 w/w) at 21 °C overnight. The protein
1438 digests were acidified (trifluoroacetic acid to 1%), centrifuged at 21,000 x g for 10 min at 4°C to
1439 remove any insoluble material, desalted with Sep-Pak C18 cartridge (Waters), and dried by
1440 Speedvac. Each sample was resuspended in 50 mM HEPES (pH 8.5), TMT labeled, mixed equally,
1441 desalted, and fractionated by offline HPLC (Agilent 1220) using basic-pH reverse phase LC (Waters
1442 XBridge C18 column, 3.5 µm particle size, 4.6 mm x 25 cm, 180 min gradient, 80 fractions).
1443 Fractions were aliquoted (5% v/v) for whole proteome and methylome (95% v/v) profiling. The
1444 methylome fractions were further concatenated into 10 fractions for antibody-based sequential
1445 mono-methyl-arginine and di-methyl-arginine peptide enrichment.

1446

1447 **Antibody-based Sequential Methylome Enrichment**

1448 Each concatenated fraction (approximately 1 mg) was resuspended in 400 µL ice-cold IAP buffer
1449 (50mM MOPS, pH 7.2, 10 mM sodium phosphate, and 50 mM NaCl) and centrifuged at 21,000 ×
1450 g for 10 min at 4°C to remove any insoluble material. The peptides were then incubated with
1451 mono-methyl-Arginine antibody beads (mono-me-R, 12235S Cell Signaling Technology) at an

1452 antibody-to-peptide ratio of 1:20 (w/w, optimized through a pilot experiment) for 2 hr at 4°C with
1453 gentle end-over-end rotation. The antibody beads were then collected by a brief centrifugation,
1454 washed 3 times with 1 mL ice-cold IAP buffer and twice with 1 mL ice-cold PBS, while the
1455 supernatants were carefully removed and used for the sequential di-methyl-Arginine peptide
1456 enrichment (di-me-R symmetric, cat.13563S Cell Signaling Technology). Peptides were eluted
1457 from the beads twice at room temperature with 50 µL of 0.15% TFA, dried, and analyzed by LC-
1458 MS/MS.
1459
1460 **LC-MS/MS Analysis**
1461 Each sample was dried, reconstituted, and analyzed by LC-MS/MS (a CoAnn 75 µm x 30 cm
1462 column, packed with 1.9 µm C18 resin from Dr. Maisch GmbH) interfaced with the Orbitrap
1463 Fusion MS (Thermo Fisher). LC settings included an 80 min gradient of 15%-40% buffer B (70%
1464 ACN, 2.5% DMSO, and 0.1% FA) with buffer A (2.5% DMSO, and 0.1% FA) at a flow rate of ~0.25
1465 µL /min flow rate. MS settings included data-dependent (3 s cycle) mode with a survey scan in
1466 the Orbitrap (60,000 resolution, scan range 410–1600 m/z, 1 × 106 AGC target, and 50 ms
1467 maximal ion time), followed by sequential isolation of abundant ions in a 3 s duty cycle, with
1468 fragmentation by higher-energy collisional dissociation (HCD, 38 normalized collision energy),
1469 and high-resolution detection of MS/MS ions in the Orbitrap (60,000 resolution, 1 × 105 AGC
1470 target, 105 ms maximal ion time,1.0 m/z isolation window, and 20 s dynamic exclusion).
1471
1472 **Database Search and TMT Quantification**
1473 The MS/MS spectra were searched against the UniProt Mouse protein database (version
1474 2020.04.22) using the COMET algorithm (v2018.013(*42*) **)** with the JUMP software suite(*43*)**.**
1475 Search parameters included MS1 mass tolerance of 20 ppm and MS/MS of 0.02 Da, fully tryptic,
1476 static mass shift for the TMT16 tags (+304.2071453) and carbamidomethyl modification of
1477 57.02146 on cysteine, dynamic mass shift for Met oxidation (+15.99491), for mono-methyl-
1478 Arginine (+14.01565), and for di-methyl-Arginine (+28.0313), maximal missed cleavage (n = 3),
1479 and maximal dynamic modifications per peptide (n=5). All matched MS/MS spectra were filtered
1480 by mass accuracy and matching scores to reduce false discovery rate (FDR) below 1% for either

1481 proteins (whole proteome analysis) or peptides (methylome analysis), based on the target-decoy
1482 strategy(*44, 45*).
1483
1484 TMT quantification analysis was performed as previously reported(*46*) with the following
1485 modifications: (i) extracting reporter ion intensities from each PSM; (ii) correcting the intensities
1486 according to the isotopic distribution of each TMT reagent; (iii) removing PSMs of very low
1487 intensities (e.g., minimum value of 1,000 and median value of 5,000); (iv) normalizing sample
1488 loading bias with the trimmed median intensity of all PSMs; (v) calculating the mean-centered
1489 intensities across samples (e.g., relative intensities between each sample and the mean), (vi)
1490 summarizing protein relative intensities by averaging related PSMs; (vii) finally deriving protein
1491 absolute intensities by multiplying the relative intensities by the grand-mean of the three most
1492 highly abundant PSMs. (vii) Protein fold change and p-values of different comparisons were
1493 calculated based on the protein intensities, using a log transformation and moderated t-test with
1494 the limma R package(*47, 48*).
1495

1496 **Quantification and statistical analysis**

1497 Data were plotted and analysed using GraphPad Prism (GraphPad Software, v.9.2.0). Statistical
1498 significance was calculated using unpaired one- or two-tailed Student's *t*-tests. Two-way ANOVA
1499 was performed to compare tumor growth curves. The log-rank (Mantel–Cox) test was performed
1500 to compare the mouse survival curves. For Fig. 4A, a linear mixed effects model with log10(y) as
1501 the response variable, group as a fixed-effect predictor variable, and mouse as a random-effect
1502 predictor variable was fit to the data. This model represents data with cells as random samples
1503 from each mouse. The results showed that the mean log10(y) values of the two mouse groups
1504 differed by -0.131 units (95% CI: -0.163, -0.0999; $p = 6.98\ 10^{-15}$). Statistical significance was set at
1505 $P < 0.05$. Data are presented as mean ± SEM. No statistical methods were used to determine
1506 sample size.

1507